AGU PUBLICATIONS

JGR

Journal of Geophysical Research: Atmospheres

RESEARCH ARTICLE
10.1002/2016JD026336

Key Points:
- The estimated GEC generator current is 1.4-1.6 kA
- The generator current varies primarily with the (semi) annual cycle and diurnal cycle, but ENSO and MJO signals are noted
- The estimated generator current varies least on decadal (7.5%) and weekly (2%) time scales and the latter is likely not a global signal

Correspondence to:
M. Peterson,
michaeljp24@gmail.com

Citation:
Peterson, M., W. Deierling, C. Liu, D. Mach, and C. Kalb (2017), A TRMM/GPM retrieval of the total mean generator current for the global electric circuit, *J. Geophys. Res. Atmos.*, *122*, 10,025–10,049, doi:10.1002/2016JD026336.

Received 5 DEC 2016
Accepted 22 AUG 2017
Accepted article online 7 SEP 2017
Published online 25 SEP 2017

A TRMM/GPM retrieval of the total mean generator current for the global electric circuit

Michael Peterson[1,2], Wiebke Deierling[3], Chuntao Liu[4], Douglas Mach[5], and Christina Kalb[1]

[1]National Center for Atmospheric Research, [2]University of Maryland, [3]University of Colorado, Boulder, [4]Texas A&M University Corpus Christi, [5]Global Hydrology and Climate Center, Universities Space Research Association, Huntsville, Alabama

Abstract A specialized satellite version of the passive microwave electric field retrieval algorithm (Peterson et al., 2015) is applied to observations from the Tropical Rainfall Measuring Mission (TRMM) and Global Precipitation Measurement (GPM) satellites to estimate the generator current for the Global Electric Circuit (GEC) and compute its temporal variability. By integrating retrieved Wilson currents from electrified clouds across the globe, we estimate a total mean current of between 1.4 kA (assuming the 7% fraction of electrified clouds producing downward currents measured by the ER-2 is representative) to 1.6 kA (assuming all electrified clouds contribute to the GEC). These current estimates come from all types of convective weather without preference, including Electrified Shower Clouds (ESCs). The diurnal distribution of the retrieved generator current is in excellent agreement with the Carnegie curve (RMS difference: 1.7%). The temporal variability of the total mean generator current ranges from 110% on semi-annual timescales (29% on an annual timescale) to 7.5% on decadal timescales with notable responses to the Madden-Julian Oscillation and El Nino Southern Oscillation. The geographical distribution of current includes significant contributions from oceanic regions in addition to the land-based tropical chimneys. The relative importance of the Americas and Asia chimneys compared to Africa is consistent with the best modern ground-based observations and further highlights the importance of ESCs for the GEC.

Plain Language Summary Electrified weather across the globe powers the Global Electric Circuit (GEC) that regulates the electrical potential of the ionosphere. As it is impossible to measure the current provided by every electrified cloud directly, we use a retrieval algorithm to quantify this current from Tropical Rainfall Measuring Mission (TRMM) and Global Precipitation Measurement (GPM) satellite measurements. We then examine the variability of this generator current on time scales that range from one day to more than a decade.We estimate that electrified weather provides an average current of 1.4 kA and 1.6 kA globally. Though current contributions can be found in land and ocean regions across the globe, large concentrations are found in the tropics near the equator and in the "tropical chimneys" of the Americas, Africa, and Asia. The greatest source of variability in the GEC generator current is on the semi-annual time scale (110%) followed by local hour (58%), and universal time (34% - Carnegie curve). The smallest variations are on the decadal (7.5%) and weekly (2%) time scales.

1. Introduction

The GEC encompasses the electrical connections in the Earth system between electrified weather, the ionosphere, and the Earth's surface. The GEC establishes a potential difference between the ionosphere and the surface of around 240 kV [*Adlerman and Williams*, 1996; *Markson*, 2007]. It has received considerable attention in the past decade [review: *Williams*, 2009; *Williams and Mareev*, 2014] due in part to its potential for monitoring climate [*Williams*, 2005] and the need to represent the planet's electrical subsystem in Earth system models [*Lucas et al.*, 2015]. Moreover, recent advances in observations make it possible to address longstanding questions on what kinds of electrified weather contribute to the GEC, how these contributions are distributed around the globe, and what factors account for its variability.

The GEC may be described simply as a Direct Current (DC) Resistor-Capacitor (RC) circuit consisting of a current source (electrified clouds) and passive electric elements [*Rycroft et al.*, 2000, 2007]. Multipole charge distributions in thunderstorms and ESCs lead to the establishment of upward- and downward- directed conduction currents depending on the charge structure of the storm. These currents are denoted "Wilson" currents in the literature after C.T.R. Wilson who proposed the first theory of a global circuit powered by

electrified weather. Wilson currents produced by electrified weather interact directly with the highly conductive ionosphere or the Earth's surface in case of downward-directed conduction currents [*Wilson*, 1920]. Upward currents are the most common, accounting for 93% of all electrified clouds measured by the NASA ER-2 aircraft [*Mach et al.*, 2010].

The overall flow of current through the GEC can be determined by integrating the Wilson current contributions from all electrified weather across the globe. This total current provided by GEC sources is termed the "generator current" to contrast the fair-weather return current. The GEC has been proposed as a "natural framework for monitoring global change on many time scales" [*Williams*, 2005] because it encapsulates changes in the frequency and intensity of electrified weather into a single system that is routinely measured. Some of the earliest observations of the GEC were taken by the research vessels *Carnegie* and *Maud*. These ships recorded the average fair-weather electric field as a function of Universal Time during their voyages across the world's oceans to establish the diurnal variation of the GEC [*Whipple*, 1929]. The resulting annual average variation given by *Israel* [1973, Appendix, Table XIX] is known as the "classic" Carnegie curve, and provides a climatology that approximates the modern measurements of the fair weather electric field in the Antarctic [*Burns et al.*, 2005, 2012, 2017] and the ionospheric potential [*Markson*, 2007]. The Carnegie curve's early 20th century origins make it a natural reference point against which to assess large-scale changes in electrified weather with the passage of time [*Harrison*, 2013]. *Burns et al*. [2017] uses a combination of electric field measurements from the Vostok and Concordia stations in Antarctica to provide considerably more accurate diurnal curves that are also resolved seasonally. These curves show changing contributions from the major northern and southern hemisphere sources as the seasons progress.

The variability of the GEC on a number of time scales has been discussed in the literature. *Rycroft and Harrison* [2012] summarize the sources of many of these. For the Direct Current (DC) variations of interest to this study ($>$ ~200 s, the RC time constant of the atmosphere), the time scales listed include: $<$ 1 day (thunderstorm cell growth, gravity waves, tidal variations), diurnal, ~5-days (planetary waves), 27-day, annual, 11-year (solar cycle), and long-term trends [*Rycroft and Harrison*, 2012]. Additional variations have also been discussed. The possibility of a weekly cycle in lightning and electrified weather has been debated [i.e. *Altaratz et al.*, 2010; *Bell et al.*, 2009; *Lyons et al.*, 1998; *Rosenfeld et al.*, 2012; *Vonnegut et al.*, 1995; *Williams et al.*, 1999]. The proposed weekly cycle is anthropogenic in origin, resulting from weekday and weekend changes in aerosol production. Variations on the intra-seasonal [Madden Julian Oscillation: *Anyamba et al.*, 2000; *Madden and Julian*, 1972], semi-annual [*Christian et al.*, 2003; *Fullekrug and Constable*, 2000; *Williams*, 1994], and interannual (El Nino Southern Oscillation) [*Dowdy*, 2016; *Hamid et al.*, 2001; *Sátori et al.*, 2009; *Williams*, 1992, 1999; *Yoshida et al.*, 2007] time scales have also been assessed. The origins of these variations are primarily attributed to adjustments to the global generator current from electrified weather following large-scale changes in temperature [i.e. *Reeve and Toumi*, 1999; *Williams*, 1994, 1999, 2005] and vertical development [*Williams*, 1985; *Yoshida et al.*, 2009].

The primary caveat to using electric field measurements for this purpose [*Burns et al.*, 2005; *Harrison*, 2002; *Märcz and Harrison*, 2003; *Markson*, 2007] is that factors unrelated to global electrified weather may affect the readings. Changes in ion concentration and mobility, involving cosmic ray and radon variations and ion attachment to aerosols and cloud droplets modify the conductivity of the atmosphere [*Baumgaertner et al.*, 2014; *Bazilevskaya et al.*, 2008; *Tinsley and Zhou*, 2006; *Williams*, 2003]. The same distribution of electrified weather may lead a surface station to measure a different fair-weather electric field if the atmospheric conductivity is sufficiently perturbed.

Explaining linkages between the variability of electrified weather and the GEC generator current across a range of time scales requires a fundamental understanding of how different types of electrified clouds interact with the GEC. It is important to know which clouds produce Wilson currents, how the strengths of those currents vary between electrified cloud types, whether the currents contribute to (upward-directed) or discharge (downward-directed) the circuit, and how these clouds are distributed across the globe. These questions are still under active discussion [see *Williams*, 2009; *Williams and Mareev*, 2014 for a review] including the questions of how much current is contributed by ESCs compared to thunderstorms [*Mareev and Volodin*, 2014], and to what extent slow transients from lightning discharges contribute to this DC branch of the GEC [*Mareev et al.*, 2008].

C.T.R. Wilson's original thesis identified ESCs alongside thunderstorms as important sources of current for the GEC [*Wilson*, 1920]. Early support for this global circuit hypothesis, however, relied on land-based thunderstorm observations alone [*Whipple*, 1929; *Whipple and Scrase*, 1936]. This focus on the tropical "chimney" regions of the Americas, Africa and Europe, and East Asia [*Williams and Satori*, 2004] resulted in a diurnal variation that agreed in phase with the Carnegie curve but had a notably greater amplitude. *Williams and Heckman* [1993] showed that this amplitude mismatch could not be explained by oceanic thunderstorms and, instead, proposed that conduction currents rather than lightning (for example, Wilson currents) drive the GEC.

Wilson currents have been measured over thunderstorms and ESCs by NASA aircraft since 1986 [*Blakeslee et al.*, 1989]. These observations have been used to construct overall statistics of current from electrified weather [*Mach et al.*, 2009], individual distributions for thunderstorms and ESCs in land and ocean regions [*Mach et al.*, 2010], and distributions by storm type and phase [*Deierling et al.*, 2014]. The aircraft data have also been used to add ESC and/or low flash rate thunderstorm contributions to the diurnal cycles of lightning measured from low-Earth orbit [*Mach et al.*, 2011] and thunderstorms detected by the ground-based World Wide Lightning Location Network [*Hutchins et al.*, 2014; *Mezuman et al.*, 2014].

These "corrections" to the diurnal cycles of lightning and thunderstorms agree well with the Carnegie curve, but they do not answer the question of how the microphysics and kinematics of electrified weather produce the Wilson currents that are measured by the ER-2 aircraft and lead to the Carnegie curve in the fair-weather electric field. *Liu et al*. [2010] revisited Wilson's original hypothesis that electrified weather contributes to the GEC by carrying negative charge to the ground through precipitation. *Liu et al*. [2010] parsed a database of Precipitation Features (PFs) in the Tropical Rainfall Measuring Mission [TRMM, *Kummerow et al.*, 1998] dataset and identified electrified cloud features in two categories: thunderstorms where lightning was observed within the feature boundaries, and ESCs where 30 dBZ echo top temperatures fall below 10° C over land or 17° C over the ocean without lightning. The diurnal variations of total rainfall and raining area from these feature categories are found to match the Carnegie curve better than the thunder day curves in *Whipple* [1929].

Wilson currents can be computed for individual electrified clouds using the electric field retrieval algorithm developed in *Peterson et al*. [2015]. This algorithm uses microphysical cloud properties to infer the electric field that would be detected by a high-altitude aircraft passing over an electrified cloud. It was constructed using coincident 85 GHz passive microwave and electric field measurements taken by the NASA ER-2 aircraft [*Mach et al.*, 2009; *Spencer et al.*, 1994]. It produces an estimate of the three-dimensional electric field vector at any location above the cloud and a specified altitude (typically the nominal ER-2 cruising altitude of 20 km) based on the spatial distribution of 85 GHz brightness temperature in the passive microwave scene. The charge structure of the electrified cloud is modeled as a geospatial grid of net charges whose relative charge concentrations and altitudes increase with decreasing 85 GHz brightness temperature. Lower brightness temperatures are indicative of more intense convection and signify a greater column ice mass that aids collisions and non-inductive charging [NIC: *Jayaratne et al.*, 1983; *Mansell et al.*, 2005; *Reynolds et al.*, 1957; *Saunders and Peck*, 1998; *Saunders et al.*, 1991; *Takahashi*, 1978; *Takahashi and Miyawaki*, 2002]. Once the relative strengths and three-dimensional positions of the charges are known, the algorithm applies Coulomb's law to approximate the electric field vector that would be measured by the aircraft.

The performance of this algorithm has been addressed using the ER-2 electric field mill measurements [*Peterson et al.*, 2015]. Wilson current densities are calculated by multiplying these retrieved electric fields by a measured or assumed atmospheric conductivity. Current densities can then be integrated geospatially to quantify the total Wilson current for the observed electrified cloud. A key feature of this approach is that it is only sensitive to the changes in electrified weather that the GEC framework is proposed to monitor. It does not respond to changes in atmospheric conductivity unless prescribed by the modeler. Since these changes in electrified weather are our primary concern, an assumed constant 20 km conductivity within the range of values measured by the ER-2 in *Mach et al*. [2009] of 2.4 pSm^{-1} is generally used.

In this study we apply the algorithm from *Peterson et al*. [2015] to global satellite passive microwave observations taken by the TRMM and GPM [*Hou et al.*, 2014; *Smith et al.*, 2007] satellites to estimate the generator current for the GEC and examine its spatiotemporal variability. Section 2 describes the technical approach employed by the algorithm and summarizes the modifications made to the algorithm for the satellite

datasets. The global mean generator current is computed in Section 3.1 and the climatological diurnal cycle is compared with the Carnegie curve and with proxies in the literature. Section 3.2 examines variations in the total retrieved current on weekly to decadal time scales. Finally, the role of current contributions from stratiform clouds is discussed in the context of these results in Section 3.3.

2. Data and Methodology

The algorithm from *Peterson et al*. [2015] is applied to observations from the two NASA Precipitation Measurement Mission (PMM) low-Earth orbit satellite platforms: TRMM and GPM. The TRMM satellite had an orbital inclination of 35° and operated for 17 years between late 1997 and mid-2015. It featured a unique sensor package that included a Precipitation Radar (PR), Microwave Imager (TMI), Visible and Infrared Scanner (VIRS), and Lightning Imaging Sensor (LIS). The instruments on TRMM that are of primary interest to this study are the PR and TMI. The PR was the first rain radar in space. It sampled across a 215 km swath with a pixel size of 4.3 km in the horizontal and 0.25 km in the vertical at nadir. The TMI was a 9-channel passive microwave radiometer. The 85 GHz channels (8 and 9) used in this study had an Effective Field of View (EFOV) of 4.6 km (cross track) and 7.2 km (down track) across a 759 km swath [*Kummerow et al.*, 1998]. With a period of 92 minutes, TRMM completed approximately 15 orbits per day. The satellite was boosted in August of 2001 from an altitude of 350 km to 403 km to extend its mission. This resulted in an increase of ~1 km in each of these horizontal footprint dimensions: 4.3 km to 5 km for PR, 5x7 km to 6x8 km for TMI 85 GHz [*Shimizu et al.*, 2009; *Shin and Chiu*, 2008].

GPM was launched in the first quarter of 2014 as a successor to TRMM and provides similar precipitation radar and passive microwave observations from an orbit that extends to ±65° latitude at an altitude of 407 km. A notable advancement with the GPM core observatory is that it features a Dual-Frequency Precipitation Radar (DPR) that combines Ku-band and Ka-band measurements. We use only the Ku-band radar in this study because its larger swath of 245 km covers a greater fraction of the 904 km GPM Microwave Imager (GMI) domain. The scan geometries of these sensors otherwise compare well with their TRMM counterparts. Both DPR radars have a 5 km horizontal resolution and 0.25 km vertical resolution similar to TRMM post-boost, while the GMI 89 GHz channel has a resolution of 6 km that is slightly finer than the TMI post-boost. One notable difference between TRMM and GPM, however, is that GPM lacks an onboard lightning sensor. This will inhibit the classification of thunderstorms (features with lightning detected) and ESC (features without lightning detected) currents, though this is not necessary for the present analysis.

2.1. Electric Field Retrieval Algorithm for the TRMM and GPM Satellites

The passive microwave electric field retrieval algorithm described in *Peterson et al*. [2015] is applied to 86,000 TRMM orbits between 12/1997 and 4/2013 and 8,600 GPM orbits between 3/2014 and 9/2015. The algorithm estimates the three-dimensional electric field that would be measured by an observer (i.e. the ER-2 aircraft) at any point within the union of the passive microwave and radar swaths in two processing steps. First, the relative geospatial distribution of cloud charge concentration is represented using a passive microwave proxy. Second, Coulomb's Law is applied to the microwave charge proxy to construct the three-dimensional electric field vector at the observer location. These proxy electric fields are converted to an estimate of the measured electric field using an empirical transfer function developed using ER-2 electric field measurements.

Both the ER-2 [*Peterson et al.*, 2015] and satellite versions of this algorithm operate on the premise that the cloud ice content 85 GHz measurements are sensitive to and can be used as a proxy for cloud charge. This assertion is supported by the NIC mechanism where collisions between graupel and small ice particles in the presence of supercooled liquid water result in a transfer of electrons from one species of ice to the other. Convective updrafts then sort these charged ice particles according to their masses and establish the charge structures that are responsible for generating Wilson currents and producing lightning flashes. Lower 85 GHz brightness temperatures signify more vigorous convection with a greater ice content, a higher potential for collisions, and more charge separation.

Charge structures observed in nature are often described in terms of a convective dipole or tripole model [*Williams et al.*, 1989]. These models account for most thunderstorms and many of the ESCs that are thought to be the primary drivers of the GEC. Some cloud types are associated with charge structures that differ from these standard models, however. Stratiform clouds in Mesoscale Convective Systems are a key example.

Stratiform charge regions are often horizontally expansive – on the order of 100 km across - and consist of two to as many as six charge layers of alternating polarity [*Lang et al.*, 2004; *Marshall and Rust*, 1993; *Marshall et al.*, 2009; *Stolzenburg et al.*, 1994].

The algorithm from *Peterson et al.* [2015] does not identify each of the individual charge regions, but rather assumes that the charge structure can be approximated as a single characteristic layer when viewed by a distant observer far above the cloud. This simplification is currently necessary for estimating the electric field at each point over the electrified cloud, but future versions will assign multiple charges based on the local radar profile. A single charge is placed in each passive microwave pixel within the boundaries of the electrified cloud. The charge layer height in the ER-2 version of the algorithm in *Peterson et al.* [2015] is assigned using a lookup table based on the local passive microwave brightness temperature. The TRMM and GPM version of the algorithm used in this study, however, determines this height from the PR or Ku-PR radar profile. The net charge in each microwave pixel is placed at the 30 dBZ echo top height that approximates the highest altitude with a graupel signature and often coincides with the lower boundary of the upper positive charge layer [i.e. *Stolzenburg et al.*, 1994, Figure 17].

Characterizing the charges based on the passive microwave signal and radar structure allows the algorithm to adjust itself to represent a large variety of storms in different seasons and parts of the world. This adaptability means that no tuning is required for land vs. ocean storms or thunderstorms vs. ESCs, as microphysical differences between electrified cloud types should already be represented in the radar and passive microwave data. The assumption of a distant observer above the cloud (the "far field" assumption) is necessary because the lack of additional charge layers in our simplified model becomes more pronounced as the observer moves closer to the top of the storm. In the extreme case where the observer is embedded within the electrified cloud, the retrieved electric fields would be meaningless.

Uncertainties caused by this simplification of a net charge layer are "built-in" to the empirical transfer functions that translate the microwave proxy into electric field values. So long as the input brightness temperatures produce electric field estimates that approximate the measurements taken by the ER-2, errors in the intermediate charge proxy are of little consequence to the retrieval. Our analysis of more than 200,000 points of comparison between the ER-2 field mills and microwave scene across a variety of storm types indicates that this methodology is robust [*Peterson et al.*, 2015].

2.2. TRMM and GPM Caveats for the Electric Field Retrieval Algorithm

The foremost difficulty with applying the *Peterson et al.* [2015] algorithm to these satellite datasets is that TRMM and GPM observe types of weather and parts of the globe that are not sampled by the ER-2 aircraft. We do not expect large errors in the satellite retrieval for TRMM and GPM cases that have a counterpart in the ER-2 overflight data, but there are several scenarios where we have no direct electric field measurements to validate the retrieval or that the algorithm was not designed to handle.

The first scenario is the case of the tallest convection observed by TRMM and GPM. The PR and DPR occasionally measure intense storms with 30 dBZ echoes that encroach upon the 20 km nominal cruising altitude of the ER-2 aircraft where we place our observer. The retrieved electric fields increase substantially due to the distance-squared term in Coulomb's law. In these cases where the far-field assumption is violated, the dynamic response of the algorithm to the local storm structure becomes a serious source of error. We impose a limit of 19 km on charge height that removes currents that are orders of magnitude greater than what is physical for a given storm, but biases still remain towards certain regions where tall convection is frequent. These regions include northern Argentina in the Americas, the Congo Basin in Africa, the Middle East, northern India and southern China in Asia, and northern Australia.

The ideal solution for removing this bias is to move the observer to a higher altitude far above tall convection. Though we lack electric field observations at higher altitudes, the total current should remain invariant regardless of the altitude chosen for the observer. In addition to the baseline run with a 20 km observer, we also run the algorithm with an observer at a constant 5 km above the dynamic charge layer height and at constant altitudes ranging from 30 km to 60 km. We then use these higher-altitude runs that are less affected by tall convection to normalize the original 20 km run to remove this bias. The total current is identical in the unmodified baseline 20 km run and each of these normalized runs. The only aspect that changes is how the electric field algorithm responds to the tallest storms relative to a typical sample of electrified clouds.

The second scenario is the case of inverted-polarity storms and electrified regions of stratiform precipitation. Though the ER-2 measures the electric field polarity, the algorithm has no mechanism for differentiating between clouds that produce upward (positive) or downward (negative) Wilson currents. The overflight data in *Mach et al*. [2009] indicates that 93% of electrified clouds produce upward-directed Wilson currents compared to 7% of the opposite polarity. *Deierling et al*. [2014] examined the same overflight data and showed that the prevalence of downward currents fluctuated based on phase of the convective life cycle (developing, mature, dissipation) and cloud type (convective, stratiform). Mature convective systems and stratiform clouds are most associated with downward currents. Inverted dipole charge structures are frequently observed in balloon soundings of trailing stratiform regions of squall lines with a maximum positive charge co-located with the radar bright band [*Shepherd et al.*, 1996]. These stratiform clouds are also known to contain anomalous positive polarity cloud-to-ground lightning flashes that are frequently associated with sprites [*Lang et al.*, 2004; *Williams*, 1998; *Williams et al.*, 2010]. Inverted dipoles are also produced during the End-Of-Storm Oscillation (EOSO) in the electric field. One explanation for this is that the electrified hydrometeors that comprise the change regions precipitate out of the dissipating storm [*Marshall et al.*, 2009].

Scenarios such as these conflict with the implicit assumption in the lack of polarity information in the *Peterson et al*. [2015] algorithm that all charge structures are net positive and all Wilson currents flow upwards. As long as there is sufficient ice in the column, the algorithm will produce a positive current, even if the cloud type in question produces a downward current or no net current at all. Representing the charge structure of stratiform precipitation is an active area of development for the algorithm. PR radar profiles and the radar bright band detection provided by TRMM 2A23 algorithm [*Awaka et al.*, 1998] that uses horizontal and vertical gradients in the PR reflectivity data to differentiate between convective and stratiform clouds may be helpful for identifying the highest concentration of charge in the column. Additionally, lightning measurements may provide an indication of the prevailing polarity of the electrified cloud. However, since this work is still in its early stages, for the time being we will consider separate runs of the algorithm that include (1) all cloud types, (2), convective clouds only, and (3) stratiform clouds only. Comparing the currents produced by each cloud type allows us to place numerical bounds on the stratiform current issue.

The third scenario is the case of microwave artifacts from terrain. The *Peterson et al*. [2015] algorithm was subject to significant ocean artifacts due to microwave emissivity differences between land and sea. The use of TMI/GMI Polarization Corrected Temperatures [PCTs: *Spencer et al.*, 1989] in the satellite algorithm solves this ocean surface problem, but the extensive domain of the two satellites introduces a new source of surface artifacts: snow cover in high altitude or mid-to-high latitude regions. Snow-covered terrain has a different emissivity in the microwave band than open terrain [*Cordisco et al.*, 2006] resulting in low 85 GHz PCTs that approximate the appearance of a large and intense convective cloud. As with the ocean previously, these artifacts must be removed using a strict filter because any pixels that remain will contaminate nearby pixels, propagating the error over a sizable area. If unchecked, these artifacts lead to unrealistic currents from the winter hemisphere.

To address this issue, PR and DPR measurements are used to distinguish between winter storms and clear air regions covered in snow. For a passive microwave pixel to be to contain cloud charge there must be a radar confirmation of rainfall near the surface [2A25 algorithm, *Iguchi et al.*, 2000]. This is the same basic requirement that *Liu et al*. [2010] used to construct their PFs before classifying them as thunderstorms and ESCs. Consequently, there are cloud types that are known to become electrified and interact with the GEC that will be missed entirely in our analysis. The most notable examples are anvil clouds that acquire charge from the convective core through advection [*Dye et al.*, 2007] and non-raining stratiform clouds whose upper and lower boundaries become electrified in response to the GEC [*Nicoll and Harrison*, 2016].

2.3. Generator Current Climatologies From TRMM and GPM Observations

Fifteen years of TRMM observations and two years of GPM observations are combined to construct climatologies of the total mean generator current for the GEC. Three sets of climatologies are produced: a 15-year TRMM-only climatology, a 2-year GPM-only climatology, and a 17-year TRMM and GPM combined climatology. These climatologies include the global distribution of the mean current provided by electrified weather as well as its temporal distributions that describe the diurnal, weekly (anthropogenic aerosol), intra-seasonal (MJO), semi-annual and annual, inter-annual (ENSO), and 15-year (TRMM) variations.

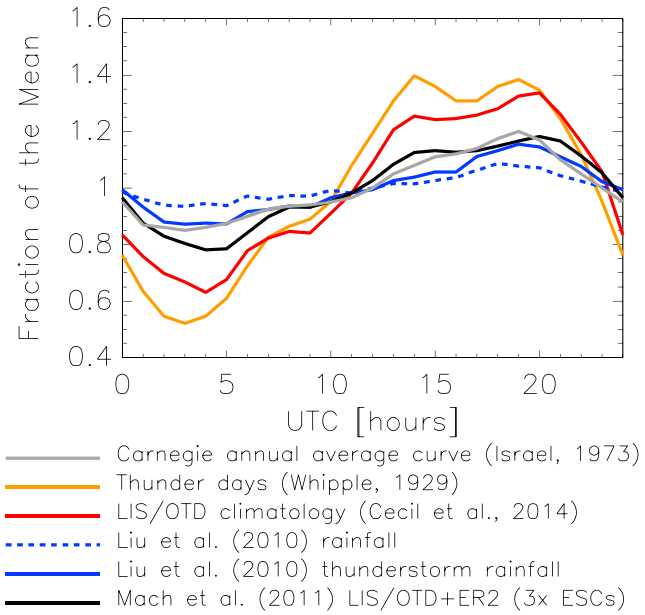

Figure 1. The Carnegie annual average curve and proxies from the literature.

As most sources for the GEC are thought to be concentrated in the tropics [*Williams*, 2009], the 15-year TRMM climatologies (tropics up to ±36°) will be used in the temporal analyses in Section 3, while the combined TRMM and GPM climatology will be used for geospatial analyses.

3. Results

Two basic quantities are required to approximate the total mean generator current for the GEC and examine its variability: the frequency of electrified weather (electrified cloud count, lightning flash rate, or total electrified cloud area) and the Wilson current contribution (or a proxy thereof) generated for each. *Liu et al*. [2010] identified electrified clouds from Radar Precipitation Features [RPFs: *Liu et al*., 2008] that met specific criteria and used the precipitation and raining area from these features to approximate the Carnegie curve. *Mach et al*. [2011] computed the mean current per lightning flash adjusted for shower cloud contributions in land and ocean regions and then used LIS and Optical Transient Detector (OTD) total lightning statistics [*Bailey et al*., 2007; *Blakeslee et al*., 1999] to estimate the total mean generator current throughout the day. *Mezuman et al*. [2014] and *Hutchins et al*. [2014] count the number of active thunderstorms around the world by clustering World Wide Lightning Location Network (WWLLN) lightning data into thunderstorm cell features and then use the ER-2 overflight data to compute the total global thunderstorm current and approximate the Carnegie curve.

Our passive microwave retrieval identifies electrified cloud pixels in TRMM and GPM observations and estimates the current density contributed by each. We calculate the total mean generator current by integrating the pixel-level currents in space and time. The retrieved electric fields have been shown to provide a reasonable comparison to ER-2 measurements for individual pixels and storm-scale features [*Peterson et al*., 2015]. Therefore, integrating these currents across the TRMM and GPM domain is expected to yield a reasonable approximation of the global mean generator current for the GEC, its spatial distribution, and its temporal variability on scales that TRMM and GPM can resolve.

Section 3.1 compares our TRMM- and GPM-derived currents with the climatological diurnal and geospatial distributions in the literature to examine where our results fall in relation to previous work. Section 3.2 then examines the temporal variability of our TRMM-derived currents from weekly to decadal time scales. Finally, Section 3.3 discusses the implications of our results for the role of stratiform clouds as current sources for the GEC.

3.1. Diurnal and Geospatial Generator Current Distributions and Comparisons With Literature

The most robust set of observations of the variability of the GEC are on the diurnal timescale. Thus, the diurnal cycle is the first hurdle that any proxy must clear if it is to have a chance at representing the general variability of the GEC. The classic Carnegie annual average diurnal variation, the LIS/OTD total lightning climatology [*Bailey et al*., 2007; *Blakeslee et al*., 1999, 2014; *Cecil et al*., 2014] and three previous approximations from the literature [*Liu et al*., 2010; *Mach et al*., 2011; *Whipple*, 1929] are compared on a common axis in Figure 1. Each of these curves has a morning minimum and evening maximum, but the amplitude and phase differs between the lightning-based curves [*Whipple*, 1929; LIS/OTD climatology] and the curves that also include ESC [*Liu et al*., 2010; *Mach et al*., 2011] in accordance with *Williams and Heckman* [1993]. The lightning-based curves also have a second peak around 14:00 UTC associated with the afternoon peak in lighting activity in the Congo basin in Africa.

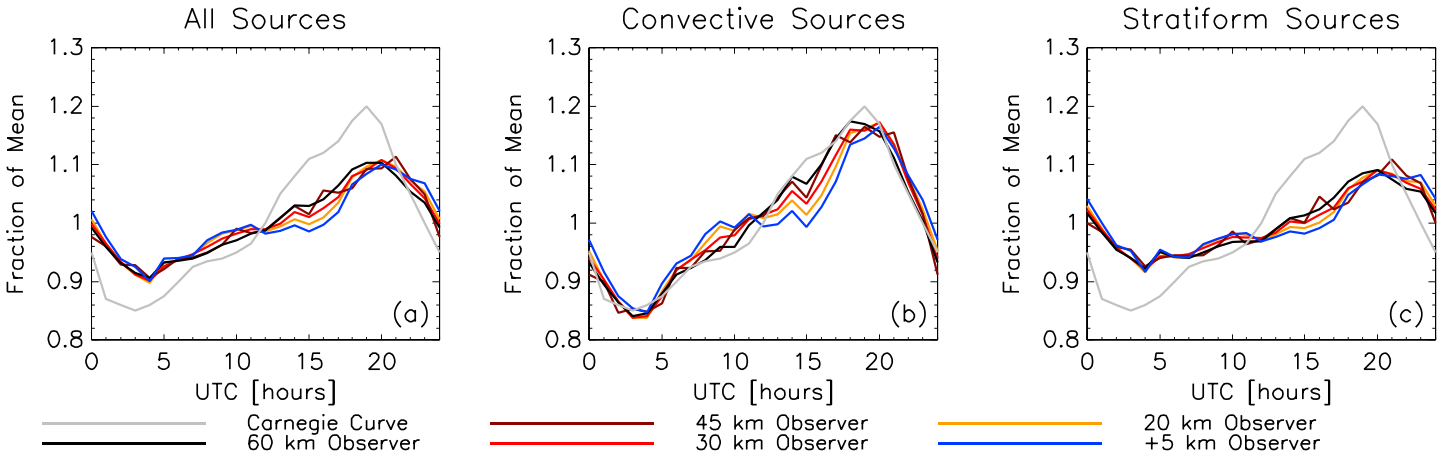

Figure 2. The Carnegie annual average curve and the diurnal distributions of total TRMM-retrieved current produced by various algorithm configurations. Individual curves are shown for each cloud type (convective and stratiform, convective only, and stratiform only) and observer height (unmodified 20 km runs or 20-km electric fields normalized by an observer at 5 km altitude above the net charge layer or a constant altitude of 30 km, 45 km, or 60 km).

Contributions from ESCs damp the lightning diurnal cycle in *Liu et al*. [2010], and *Mach et al*. [2011] and related approaches [i.e. *Hutchins et al.*, 2014; *Mezuman et al.*, 2014]. Though these curves are in a better general agreement with the Carnegie curve than *Whipple* [1929] and the LIS/OTD climatology, they come with notable caveats attached. Of the two *Liu et al*. [2010] curves plotted in Figure 1, thunderstorm rainfall best matches the amplitude of the Carnegie curve. The total rainfall curve has a single peak, but it is overdamped due to the null effect of warm rainfall. This results in an amplitude that is notably smaller than the Carnegie curve. Meanwhile, the best agreement between the *Mach et al.* [2011] curves and the Carnegie curve is achieved when it is assumed that the ER-2 aircraft undersamples ESCs and that their observed contributions should be increased by a factor of 3.

The cycles of the total generator current retrieved from TRMM measurements are compared with the Carnegie curve in Figure 2. There are 15 possible configurations of the retrieval algorithm considered. We can assume that all cloud types produce Wilson currents, that only convective clouds produce Wilson currents, or that only stratiform clouds produce Wilson currents. We can also use the unmodified baseline 20 km run or we can use a normalized run that that counteracts biases from tall storms. Possible normalizations use an observer at a constant 5 km above the charge layer or at a fixed altitude of 30 km, 45 km, or 60 km. These curves demonstrate how the algorithm responds to our assumptions and indicate which configurations provide the best approximation to the classic Carnegie curve.

All of the TRMM-derived current curves in Figure 2 bear a general resemblance to the Carnegie curve, but there are differences between configurations of the algorithm. The most significant differences come from the cloud types that are allowed to count as current sources. All sources (Figure 2a) and runs with only stratiform sources (Figure 2c) have an amplitude that is too small and a peak that is ~1 hour delayed compared to the Carnegie curve. Despite modest current contributions per pixel, the sheer number of stratiform cloud pixels from mesoscale features dominates the diurnal cycles to the point that the curves in Figure 2a and Figure 2c are nearly identical in phase and amplitude.

The convective-only runs provide the best match for the Carnegie (Figure 2b). Tthe net current contribution from all stratiform clouds is assumed to be zero in these configurations. The baseline 20 km run and the normalized runs have current distributions with the same phase and amplitude. Any of these configurations also compares better with the Carnegie curve than *Whipple* [1929] and the LIS/OTD climatology curves. The primary difference between these configurations is the shape of the distribution between the 03:00 UTC minimum and the 19:00 UTC maximum. The normalizations that are closest to the baseline 20 km run (+5 km, 30 km) and most affected by tall convection have the highest current fractions of all runs between 07:00 and 10:00 UTC. This is a time period when the Asia chimney region is most active. They also have the lowest current fractions of all runs between 13:00 and 16:00 UTC when the Africa chimney region is most active. The microphysical properties of the electrified clouds are identical in each of these runs. Thus, the differences

Table 1. Root Mean Square and Maximum Differences From the Classic Carnegie Annual Average Curve for Proxies in Literature, Approximations Used by the Frontiers in Earth System Dynamics Electrical Connections and Consequences Within the Earth System Project, and TRMM-Derived Currents (Various Algorithm Configurations are Considered)

	RMS Difference from Carnegie [%]	Max. Difference from Carnegie [%]
Literature		
Whipple [1929]	19.9	33.4
LIS/OTD Climatology	13.2	23.3
TRMM Thunderstorm+ESC Counts	8.3	14.0
Mach et al. [2011] LIS/OTD+ER2	4.4	11.0
Liu et al. [2010] Thunderstorm+ESC Rainfall	4.1	9.0
Mach et al. [2011] LIS/OTD+ER2 (3x ESCs)	3.4	6.9
Liu et al. [2010] Thunderstorm Rainfall	3.3	6.4
FESD-ECCWES		
New Mean	6.9	10.8
Median	6.6	10.4
Original Mean	6.5	10.6
Electric Field Retrieval Configurations		
20 km Unmodified Convective+Stratiform	6.7	11.2
20 km Normalized by +5 km Run Convective	4.9	11.6
20 km Unmodified Convective	3.8	9.6
20 km Normalized by 30 km Run Convective	2.9	7.7
20 km Normalized by 45 km Run Convective	2.1	5.4
20 km Normalized by 60 km Run Convective	1.7	4.2

in these curves result exclusively from the algorithm's differing sensitivity to the geometry of the problem between typical and tall convective cases. The agreement with the Carnegie curve improves with higher observer altitudes used in the normalization (i.e. when the storm is placed in a more distant field relative to the observer).

The diurnal cycles from our total generator current estimates are compared with the proxies for the generator current in the literature in Table 1. Each curve is converted to units of the fraction of its diurnal mean and then Root Mean Square (RMS) and maximum difference values are computed from the diurnal cycle of the fair-weather electric field. We use the classic Carnegie annual average curve in this analysis for consistency with past comparisons [i.e. *Mach et al.*, 2011]. This could be replaced with modern measurements from Antarctica for greater accuracy [*Burns et al.*, 2017].

RMS errors for the proxies from the literature range from 20% [*Whipple*, 1929] to 3.3% [*Liu et al.*, 2010: thunderstorm rainfall] while maximum differences range from 33% to 6.4%. Global currents used by the Frontiers in Earth System Dynamics (FESD) Electrical Connections and Consequences within the Earth System (ECCWES) project [*Kalb et al.*, 2016; *Lucas et al.*, 2015] have RMS difference between 6 and 7% and maximum differences around 10%.

Our TRMM-derived current from the baseline run with convective and stratiform current contributions, by comparison, produces an RMS difference of 7% and a maximum difference of 11% from the Carnegie curve. As in Figure 2, these differences are substantially reduced in the convective-only runs where RMS errors start at 4.9% for an observer at a constant 5 km above the net charge layer and decrease from there. The baseline 20 km run with only convective current contributions produces an RMS error of 3.8% with a maximum difference of 10%. These are similar error statistics to the total rainfall curve in *Liu et al.* [2010] that includes contributions from both thunderstorms and ESCs and the original (1x ESC in Table 3) curve from *Mach et al.* [2011]. The retrieval configuration that produces the best fit to the Carnegie curve is the 60 km normalized run with only convective contributions counted. This run produces a RMS error of 1.7% and a maximum error of 4.2%, the lowest of all proxies in Table 1.

Though each of the curves in Figure 1 and Table 1 approximates the Carnegie curve, the various approaches produce different pictures of how current sources are distributed across the globe. Studies that approximate the Carnegie curve using lightning and thunderstorm observations [*Whipple*, 1929] generally resemble the LIS/OTD satellite lightning climatology depicted in Figure 3. Lightning occurs more frequently over land than over the ocean, and is most frequent in certain key regions of the world that include Lake Maracaibo in Venezuela, the Congo Basin in Africa, certain areas of the foothills along the Himalayas in India and

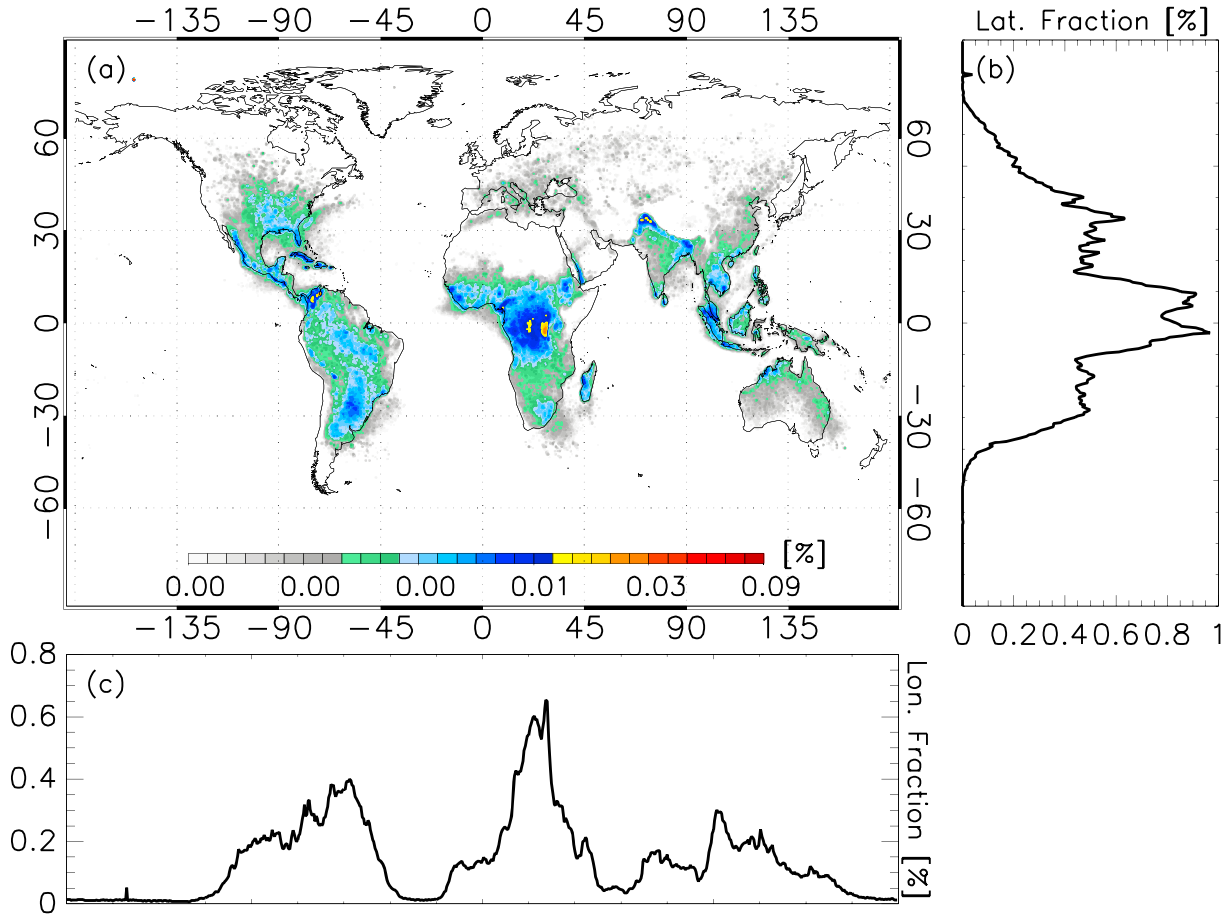

Figure 3. Global (a), latitude (b), and longitude (c) distributions of total flash rate from the LIS/OTD satellite lightning climatology.

Pakistan, and Indonesia and Malaysia in the Maritime Continent. *Albrecht et al.* [2016] ranked these hotspots using a very high resolution (0.1°) LIS climatology and found that the Lighthouse of Maracaibo outshines all other hotspots. As a function of latitude (Figure 3b), the majority of lightning activity occurs in the tropics adjacent to the massive upwelling of the Intertropical Convergence Zone where solar radiation can reach the surface and destabilize the atmosphere.

Lightning is prevalent to a lesser extent in the outer tropics and mid-latitudes, but infrequent in the high latitudes due to the Clausius-Clapeyron relationship. As a function of longitude (Figure 3c), the lightning distribution has three distinct peaks that correspond to the tropical chimney regions (the Americas, Africa and Europe, and Asia). Comparably few flashes occur outside of these regions, and, with a few key exceptions (i.e. Tahiti), lightning is uncommon in oceanic regions. Proxies that assume Wilson current strength is related to lightning and thunderstorm activity would consider these regions to be of little importance to the GEC.

By contrast, proxies that can detect ESC's [*Liu et al.*, 2010; our TRMM-retrieved currents] include significant contributions to the generator current from land and ocean. The global distribution of the total mean current provided by all cloud types in the baseline 20 km run is shown in Figure 4. This figure is a composite of TRMM and GPM observations. As a result, the sample size differences between the two satellites can be noted near the northern and southern boundaries of the TRMM domain. However, the latitude (Figure 4b) and longitude (Figure 4c) distributions are similar between the combined and TRMM-only climatologies. Many of the same regions from the LIS/OTD distribution (Figure 4a) are evident in this approximation including the three prominent chimney regions (Figure 4c). However, they are joined by significant current contributions from the tropical Pacific and Indian Oceans as well as the Gulf of Mexico and along the Gulf Stream.

The global distributions of our TRMM- and GPM-retrieved currents differ based on the cloud types and whether an observer altitude-based normalization is applied. In contrast to Figure 4 where currents from

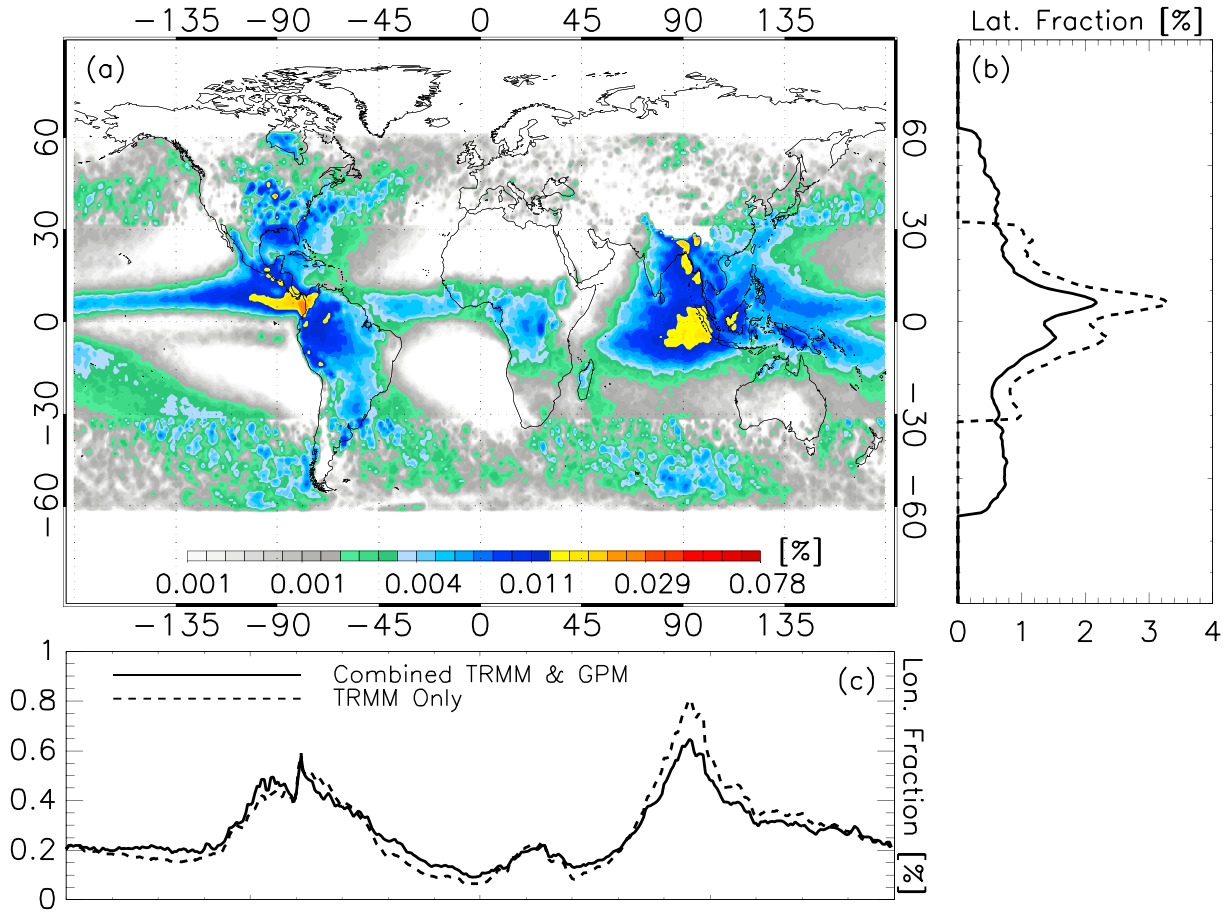

Figure 4. Global (a), latitude (b), and longitude (c) distributions of the mean TRMM-retrieved current from the baseline 20 km run constructed using TRMM PR/TMI and GPM DPR/GMI measurements of all cloud types. In contrast to lightning, the Americas and Asia chimneys contribute more current than the Africa and Europe chimney in Figure 3.

the baseline 20 km run and all cloud types are used, Figure 5 shows the global mean current distribution for the 60-km normalization and only convective current sources. Both distributions place the majority of the generator current in the tropics, but with slight distinctions in the distribution of current by longitude. The Americas (~90° W) and Asia (90° E) chimneys from Figure 4 are notably eroded in the normalized run while significant contributions from the Africa (~0° E) chimney are added. Outside of the tropics, the baseline run produces significant current up to 60 degrees latitude. Most of these sources are non-convective clouds over the Gulf Stream and Kuroshio Current. The focus on convection in Figure 5 removes these sources and the total current tapers off to zero in the high-latitudes. The normalized run with a focus on convective cloud types results in a global distribution that is more in line with the lightning climatology in Figure 3, but still includes significant contributions from both land and ocean sources.

TRMM and GPM estimates of the total global mean generator current for the GEC are shown in Table 2 Currents are calculated for TRMM only (extrapolated to high latitudes, 15 years), GPM only (2 years), and combined TRMM+GPM (17 years in tropics, 2 years elsewhere). Previous studies have estimated that the total mean current ranges from 0.75 kA to 2 kA [*Roble and Tzur*, 1986]. If we include both convective and stratiform sources, the retrieval estimates a total current of 2.1 kA to 2.3 kA. From the relatively poor fit to the Carnegie curve, we assume that much of this current is an overestimation from the unrealistic stratiform current contributions. This appears to be more of an issue with the TRMM dataset than with GPM. The TRMM extrapolation produces 740 A coming from stratiform clouds compared to 299 A in the GPM-only estimate. These convective and stratiform totals serve as upper bounds to the mean generator current we can expect from the satellite retrieval.

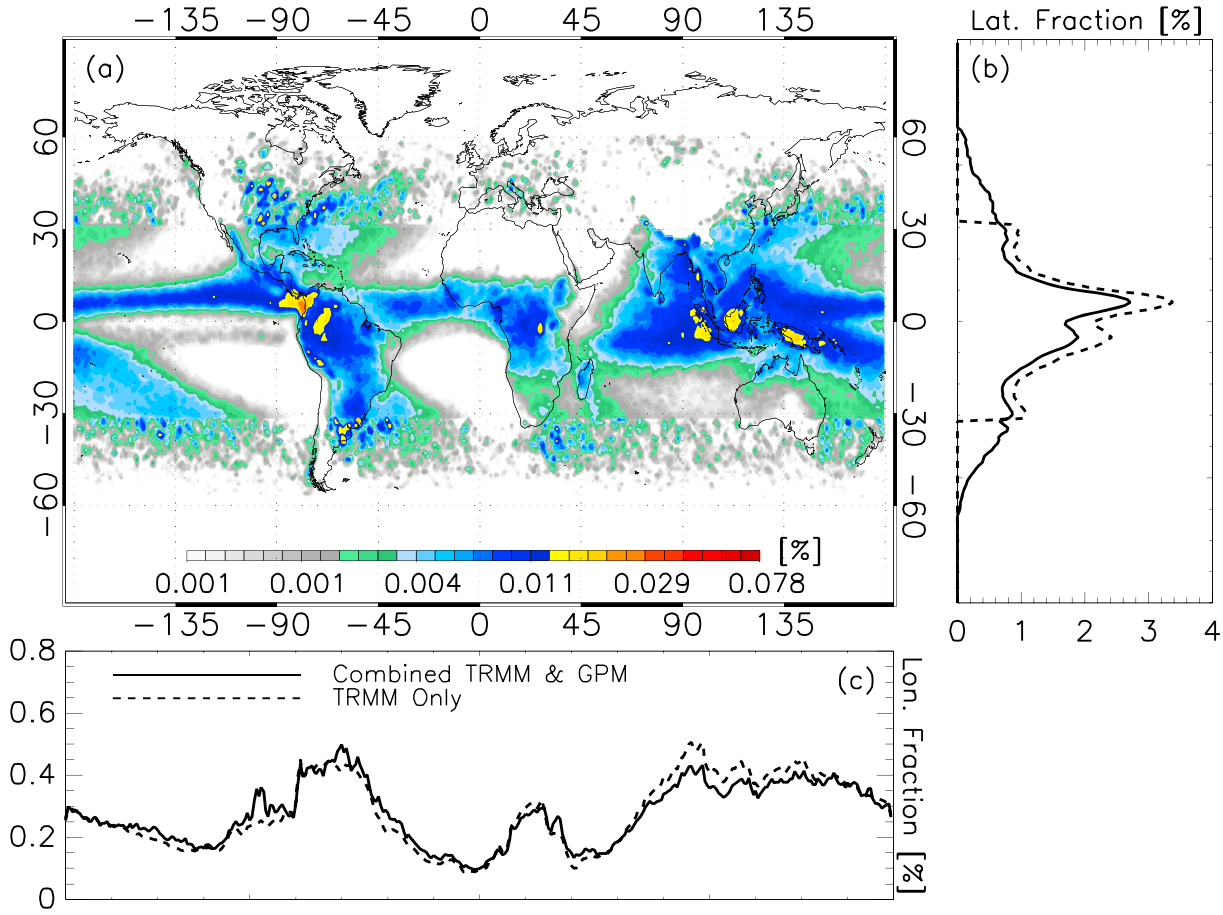

Figure 5. The same as Figure 4, but using a 60 km normalization to counteract biases from violations of the far field assumption and with only currents from convective cloud types.

We have increased confidence in the convective-only runs because they provide the best representation of the Carnegie curve. The total generator current from these runs varies between 1.6 kA and 1.8 kA, well within the range described in literature. These values would likely change with the current polarity taken into consideration. If we assume that the 7% fraction of storms measured by the ER-2 that produce downward-directed currents is representative, then we expect the total generator current to be around 1.4 kA. This is closer to the result of 1.15 kA of *Tinsley and Zhou* [2006] based on detailed conductivity profiles and measured ionospheric potential.

For the remainder of this study, only the optimal configuration of the algorithm that produces the best agreement with the Carnegie curve and previous results in the literature will be considered (convective sources only, normalized using a 60 km observer).

Table 2. The Total Global Mean Generator Current Provided by Electrified Weather Estimated From TRMM and GPM Measurements

	TRMM Only Total Current [A]*	GPM Only Total Current [A]	TRMM & GPM Total Current [A]
All	2,331	2,131	2,308
Convective	1,591	1,832	1,616
*with 7%** $\downarrow I_w$*	*1,368*	*1,575*	*1,390*
Non-Convective	740	299	692

*Extrapolated to the high latitudes.
**Fraction of overflights with downward Wilson currents from *Mach et al.* [2010].

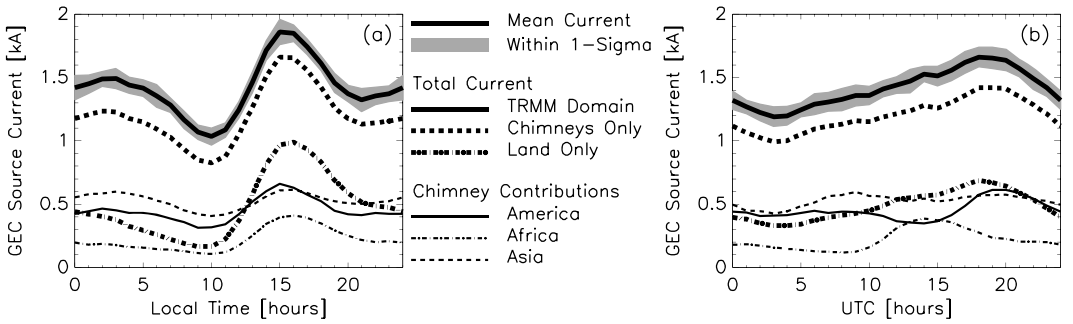

Figure 6. Diurnal variations of TRMM-retrieved current as a function of (a) local time and (b) Universal Time. Contributions from the chimney regions of the Americas, Africa, and Asia and from land only are also shown. Hourly 1-sigma values are indicated in grey.

3.2. Temporal Variations of the Retrieved Generator Current

One of the reasons the GEC has received significant attention in the past decade is that its sensitivity to changes in global electrified weather makes it a unique diagnostic tool for the overall state of the atmosphere. Changes in the frequency and intensity of convection in response to variations in temperature and large-scale dynamics should be represented in global measurements of atmospheric electricity. The following sub-sections will compute the temporal variability of the TRMM-retrieved generator current.

3.2.1. Diurnal Cycles of the Retrieved Generator Current

The response of the GEC to temperature can be demonstrated by looking at the local hour and universal time diurnal cycles of the TRMM-retrieved generator current in Figure 6. The diurnal variation of the total mean current provided by electrified weather across the TRMM domain (i.e. not extrapolated) is shown alongside individual contributions from land only and each of the three tropical chimney regions. These include the Americas (140° W – 30° W), Africa (10° W – 60° E) and Asia (60° E – 160° E). Our definitions of the chimneys use longitude ranges rather than terrain masks around the tropical land masses [*Whipple*, 1929; *Williams and Mareev*, 2014] due to significant contributions from oceanic storms in Figures 4 and 5. The sum of all contributions from the chimney regions is represented by the thick dashed line in Figure 6. The difference between this curve and the all currents curve represents the contributions from the remaining longitudes.

All of the curves in Figure 6a have a maximum between 15:00 and 16:00 local time that corresponds to peak thunderstorm activity in response to diurnal heating. A secondary peak in the early hours can be found for the global distribution and the Americas and Asia chimney regions due to the influence of MCSs and oceanic storms that have a delayed diurnal cycle relative to ordinary convection over land. These diurnal cycles are consistent with the literature on continental convection [*Hendon and Woodberry*, 1993; *Liu and Zipser*, 2008; *Nesbitt and Zipser*, 2003]. If we then map these local-hour diurnal cycles onto Universal Time coordinates, we can show the hourly contributions from the various chimneys. The maxima of the chimney curves are not aligned temporally as in Figure 6a with the local-hour curves due to their ~90° separation in longitude. The primary Asia peak occurs at 9:00 UTC (though a secondary peak is present at 20:00 UTC due to oceanic convection, also noted in Figure 6a), while the Africa peak occurs at 14:00 UTC and the Americas peak occurs at 20:00 UTC.

It is the sum of these curves and the Pacific Ocean quadrant (not included in the all chimneys curve) that determines the total current for a given hour and results in our good approximation to the Carnegie curve in Table 2. This stands in contrast to the earlier thunderstorm-based proxies [i.e. the *Whipple*, 1929 thunder area curve] where one dominant chimney controls the shape of the curve at a given hour. The 18:00 UTC peak in the global distribution of Figure 6b, for example, contains nearly equal contributions from the afternoon Americas peak (15:00 local time in Figure 6a) and the morning Asia peak (3:00 local time in Figure 6a). The 3:00 UTC minimum of the total generator current, on the other hand, occurs when the Sun is over the Pacific Ocean and corresponds to the absolute minimum in the Asia chimney curve and a local minimum between the afternoon and early morning Americas peaks from Figure 6a. No distinct maximum is evident at 14:00 UTC in Figure 6b due to the reduced amplitude of the Africa chimney compared to the LIS/OTD climatology. Though this time period (~14:00 UTC) is associated with Africa, Asian shower clouds and oceanic

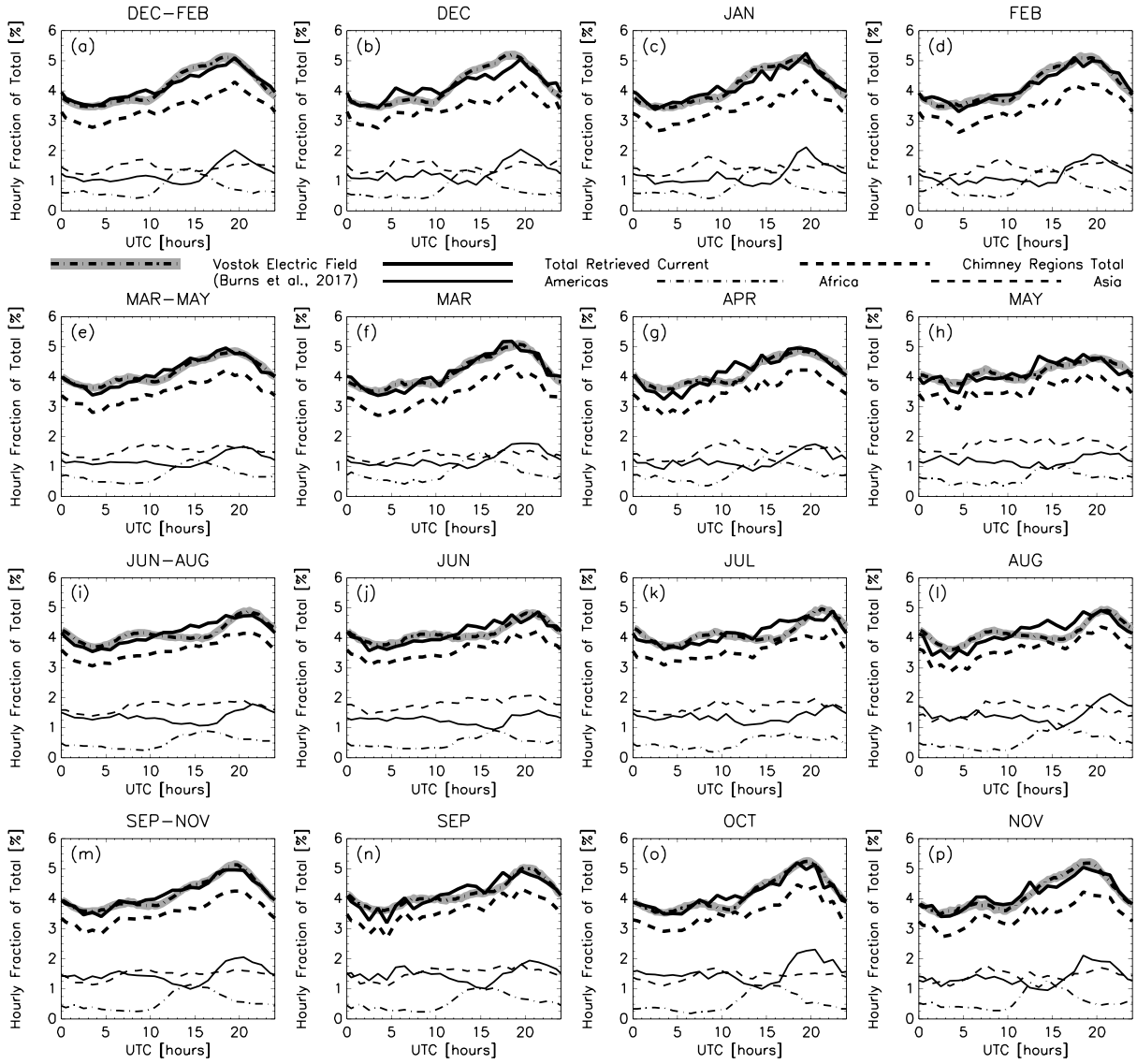

Figure 7. The diurnal variations of the mean fair-weather electric field measured at Vostok station, Antarctica [*Burns et al.*, 2017] and TRMM-retrieved current for each 3-month season (left column) and each month (right three columns). Standard errors included in the *Burns et al.* [2017] dataset are shaded in grey.

thunderstorms contribute enough retrieved current that the Asia chimney has a larger contribution than African thunderstorms during these hours.

The difference between the land-only (dot-dashed) and global total curves in Figure 6b is also notable. As in *Peterson et al.* [2015], we distinguish land and ocean regions precisely at the coastline. If we only considered land-based convection as the primary driver of the GEC, we would still arrive at a diurnal cycle that resembles the Carnegie curve, but with a reduced total current and a 50% greater diurnal amplitude than if oceanic sources are included.

The curves in Figure 6 are based on a climatology of TRMM-retrieved currents from all seasons. The diurnal response of the GEC is known to change throughout the year, however [i.e. *Blakeslee et al.*, 2014; *Burns et al.*, 2005, 2012, 2017; *Liu et al.*, 2010]. Figure 7 shows the same diurnal cycles of retrieved current separated by season and compared with ground-based electric field observations taken at Vostok station, Antarctica [*Burns et al.*, 2017]. For each season (row), the three-month average is shown in the left column and the individual monthly averages are shown in the remaining three columns to the right.

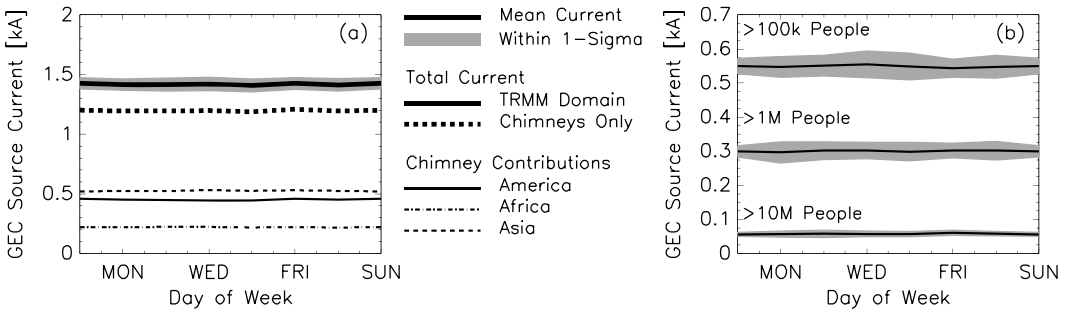

Figure 8. Weekly variations in TRMM-retrieved current for (a) the TRMM domain and each chimney and (b) land regions with populations greater than 100,000 people, 1,000,000 people, and 10,000,000 people. Daily 1-sigma values are shown in grey.

The amplitude and phase of the retrieved generator current diurnal cycle tracks with the Vostok electric field measurements throughout the year. Despite different temporal domains (2006-2011 for Vostok compared to 1998 – 2013 for TRMM) and sampling rates (continuous Vostok measurements on fair-weather days compared to TRMM snapshots of thunderstorms and ESCs), the TRMM-retrieved generator current closely matches the Vostok curve in each panel of Figure 7. Our approximation of the generator current for the GEC thus matches the variation of the fair-weather electric field in terms of the classic annual average Carnegie curve (Table 1) and modern measurements that take into account how it varies seasonally and from month to month (Figure 7).

Seasonal changes to the Vostok distributions are attributed to solar heating of the tropical chimneys. These curves shift between an earlier peak in the 19:00 hour in December to February and a delayed peak after 21:00 UTC in July and August. This UT shift is thought to result from the shape of the American landmass. The geographic center of the American quadrant of the TRMM domain north of the equator lies at 86.5° W longitude. By comparison, the geographic center of the southern hemisphere American octant lies at 58.5° W. Assuming the local hour curves are nearly identical in phase (Figure 6a) and low-latitude sources in the summer hemisphere dominate the total current (Figure 5b), then we would expect this 28° longitude displacement to cause the peak of the Americas chimney to drift by approximately 2 hours between January and August. Consistent with these predictions, the January peak in the Americas curve in Figure 7c (solid thin line) occurs at 19:00 UTC while the August peak in the Americas curve in Figure 7l occurs at 21:00 UTC, two hours later.

3.2.2. Weekly Variations of TRMM-Retrieved Generator Current

The mechanism for a weekly cycle in thunderstorm and lightning activity is tied to anthropogenic aerosol production and weekly patterns of human activity. Increased aerosol production during the workweek invigorating convection may lead to a "weekend effect" of suppressed lightning and severe weather. This idea has been debated since at least the mid 1990's [see *Williams and Mareev*, 2014 for a review] and recent studies indicate that there may be significant changes in lightning [*Bell et al.*, 2009], rainfall [*Bell et al.*, 2008], hail and tornadoes [*Rosenfeld and Bell*, 2011] over the course of the week.

Weekly distributions of TRMM-retrieved current are shown in Figure 8. The first distribution (Figure 8a) shows the weekly cycle of the total generator current throughout the TRMM domain. The total current changes by around 2% over the course of the week. It is slightly higher for the Americas (3%), but is still hardly apparent in the distribution. Given the 1-sigma values in Figure 8a (grey area), these weekly variations fall within the error bars of the retrieval and are not likely to be robust.

However, the proposed source for this variation is based on human activity. Therefore, it should be most pronounced near dense population centers. The LandScan dataset was developed as a global population database for assessing populations at risk from hazardous events such as chemical and radiation leaks as well as natural phenomena like severe weather and hurricanes [*Dobson et al.*, 2000]. We identify regions with certain population thresholds (100,000, 1,000,000, 10,000,000) in 2-degree bins in the LandScan 2010 global population dataset and examine the weekly cycle of TRMM-retrieved current in those areas. Population density should correlate with higher anthropogenic aerosol production and a more pronounced weekly cycle. Indeed, the amplitude of the weekly variation is increased for these specific regions in Figure 8b. The

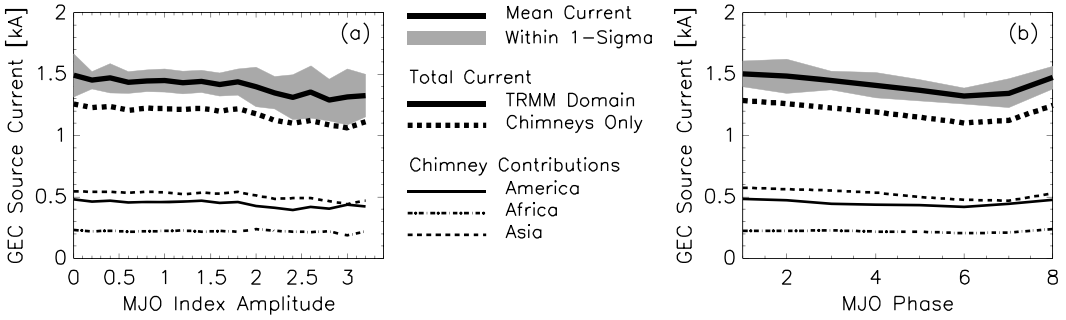

Figure 9. Variations in TRMM-retrieved current with the amplitude (a) and phase (b) of the Madden-Julian Oscillation. 1-sigma values are shown in grey.

variation for all regions with 100,000 people is 3% and regions with 10 million inhabitants or more are associated with a weekly cycle more than twice as strong at 7%. These weekly variations over the most populated parts of the world (> 10 million inhabitants) are roughly half as large as the ~15% weekly variation of lightning presented in *Bell et al.* [2009] that only accounts for thunderstorms. Moreover, these signals are small compared to the sigma values that accompany them.

The differences between the TRMM-retrieved generator current and *Bell et al.* [2009] may be related to ESC contributions that are not apparent in the lightning observations or a tradeoff between the frequency, size, and rigor of thunderstorms. Our overall assessment of the weekly cycle in the GEC generator current is that we do not find a clear weekly signal in the generator current data and if this time scale is, indeed, a robust source of variability for the GEC, then it is likely only evident at local scales. We do not expect there to be a strong global signal from this effect.

3.2.3. TRMM-Retrieved Currents and the Madden-Julian Oscillation

The Madden-Julian Oscillation [MJO: *Madden and Julian*, 1972] is the next longest time sale that we consider with a 30-60 day period. Lightning activity can vary by as much as 50% based on the amplitude and phase of the MJO [*Anyamba et al.*, 2000; *Williams*, 2005]. TRMM-retrieved current responses to both aspects of the MJO propagating wave are quantified using the Realtime Multivariate MJO (RMM) Index [*Wheeler and Hendon*, 2004] in Figure 9. This analysis is similar to the diurnal or weekly variations shown previously, but substituting local and universal time hour with MJO amplitude (0 – 3.5) or phase (1 - 8).

Stronger MJO events are associated with a general decrease in generator current for the GEC (Figure 9a), though this is accompanied by an increased standard deviation in the total current and a greater uncertainty. The MJO phase (Figure 9b) is related to the migration of organized MCSs from the ocean to the continents that may lead to different lightning flash rates and current contributions. Total currents reach a maximum under phase 1 conditions (Africa) and a minimum under phase 6 conditions (Western Pacific). Most of the variations lie in the Americas and Asia chimney regions, while non-chimney contributions remain relatively constant for all MJO amplitudes and phases. The overall response of the TRMM-retrieved generator current to the MJO is between 10-15%.

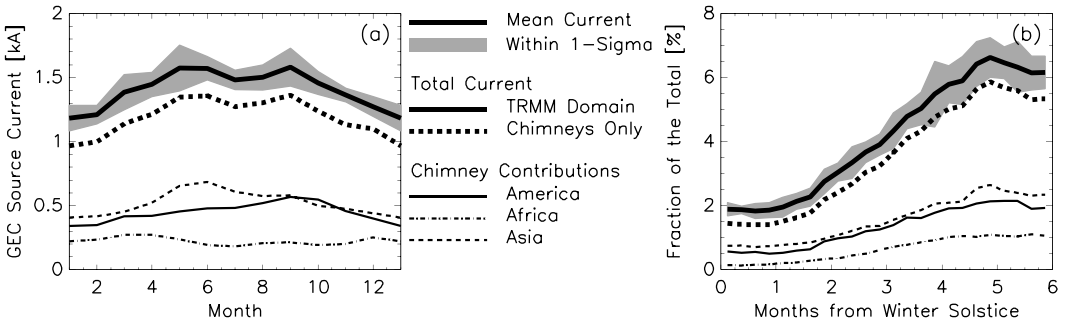

Figure 10. Annual (a) and semi-annual (b) variations in TRMM-retrieved current. 1-sigma values are shown in grey.

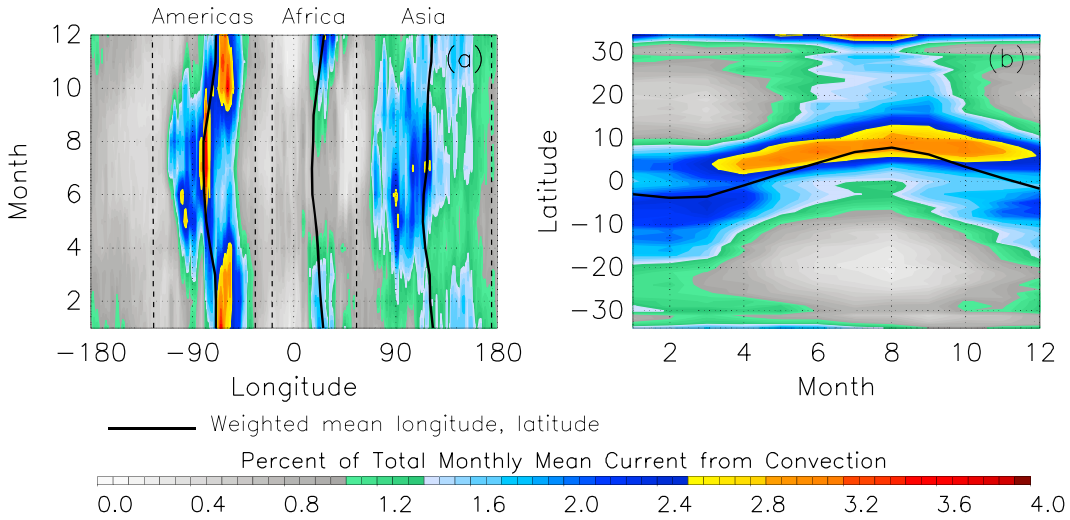

Figure 11. Two-dimensional histograms showing the change in the distribution of sources by longitude (a) and latitude (b) by month. The total for each month is 100%.

3.2.4. Seasonal to Annual Variations of TRMM-Retrieved Generator Current

The annual and semi-annual cycles of TRMM-retrieved generator current are shown in Figure 10. The total current reaches a maximum in the northern hemisphere summer and a minimum in January with an annual variation of around 30%. This variation is of a similar scale as the surface-based electric field measurements summarized in *Williams* [2009] that ranges from 21% - 28%.

The semi-annual enhancement is associated with a ~1 °C increase in temperature across the tropics [*Williams*, 1994, 2009], which equates to roughly 14% of the temperature change between summer and winter means within the TRMM domain. We assess the overall response of the GEC generator current to the passing of the seasons by distributing retrieved Wilson current contributions according to the length of time from the local winter solstice (Figure 10b). December currents in the northern hemisphere are added to July currents in the southern hemisphere, and so on. These distributions have a considerably greater amplitude and, like the local hour curves in Figure 6a, all chimney regions align in phase with the global distribution. The overall semi-annual response in the total current is 110% from winter to summer solstice.

Much of the discussion of the annual variation of the GEC has been dedicated to changes in the geographical source distribution throughout the year and the effect this has on the tropical chimneys. The shift in the peak of the *Burns et al.* [2017] electric field data from 19:00 UTC in December to February to 21:00 UTC in July September has been attributed to the westward protrusion of the North American continent relative to South America. The lowest annual values of the 3:00 UTC minimum November, December, and January are similarly attributed to a greater distance in longitude between Asia and South America than between Asia and North America.

We examine how the global distribution of sources changes throughout the year by computing the distributions of TRMM-retrieved current by latitude from Figure 5b and by longitude from Figure 5c for each month of the year. Annual changes in the current distributions are shown in Figure 11 as two-dimensional histograms of TRMM-retrieved current between longitude and month (Figure 11a) and month and latitude (Figure 11b) that are scaled so the total for each month is 100%. Additionally, we compute the monthly weighted mean longitude for the current contributions in each of the chimneys (Figure 11a, solid lines) and the monthly weighted mean latitude for the total current (Figure 11b).

The change in the longitude range for the Americas chimney is evident in Figure 11a. While the peak current between June and September lies immediately east of 90° W, it migrates eastward to near 60° W from October to March. Changes in the position of the Africa and Asia chimneys throughout the year are less pronounced. The westward progression of the Africa current during the northern hemisphere summer is only evident in the weighted mean longitude. The maximum current contributions from the Africa chimney occur during the rainy season of the Congo basin that lasts from September to April. Over Asia, the westward migration can be seen in the 1.5% contour level that is located over the Maritime Continent and Australia during

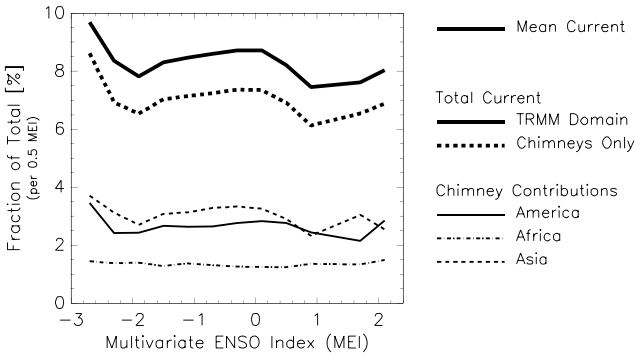

Figure 12. Variations in TRMM-retrieved current with the Multivariate ENSO Index.

the northern hemisphere winter but extends westward across India from April to September. The intensification of the Asia current during the northern hemisphere summer follows the development and life cycle of the south Asian monsoon [*Romatschke and Houze*, 2011] and the peak in lightning production over the Maritime Continent [*Christian et al.*, 2003].

Another feature of the annual cycle is a bi-modal peak in the northern hemisphere warm season. This behavior has been noted in the literature [*Burns et al.*, 2005; summarized in *Williams*, 2009] and is attributed to a bi-annual enhancement of tropical convection as the Sun crosses the equator [*Williams*, 1994]. The annual cycle in Figure 10a has a peak in May and another in September. Only the latter is aligned with an equinox. Semi-annual enhancements at 3 months from the local winter solstice are not evident in Figure 10b, however.

The May and September maxima appear to coincide with the peak for a specific chimney rather than an overall enhancement across the entire tropical belt. The May peak is associated with a prominent Asia chimney in Figure 10 while the September peak coincides with a peak in the Americas chimney. These months have a similar distribution of sources by longitude in Figure 11a. A broad Americas peak is formed by current contributions from both North and South America, the Africa chimney is in flux between its December maximum and July minimum, and the maximum of the Asia peak falls in longitudes associated with Bangladesh to western Indonesia. The key difference between the two peaks is that a greater fraction of the total current is concentrated in Asia in May while more current is concentrated in the Americas in September.

Spring contributions from both the northern and southern hemispheres can be noted in the current distribution by longitude (Figure 11a) and the current distribution by latitude (Figure 11b). These combined currents do lead to a local enhancement in the current contributions from the Americas and Asia near the spring (Americas) and fall (Asia) equinoxes in Figure 10a. However, this effect appears to be of second order and is not evident in Figure 10b at 3 months from local winter solstice. Changes in the latitude distribution of total retrieved current (Figure 11b) are also not symmetrical around the June solstice. Equatorial sources in the northern hemisphere are the primary contributors to the total generator current from March to December while southern hemisphere equatorial sources make up the largest portion of the generator current from January to March.

3.2.5. TRMM-Retrieved Currents and the El Nino Southern Oscillation

The El Niño Southern Oscillation [ENSO: *Philander*, 1990] is regarded as the single strongest source of interannual variability in the atmosphere and has profound effects on convection, rainfall, and electrified weather. These aspects are summarized in *Williams and Mareev* [2014]. El Niño events are generally associated with reduced rainfall and less frequent thunderstorms over land [*Allen et al.*, 1996]. These storms tend to be stronger, however, and the net effect is an increase in lightning activity in El Niño events compared to La Niña events [*Hamid et al.*, 2001; *Price*, 2009; *Sátori et al.*, 2009; *Williams*, 1992; *Yoshida et al.*, 2007]. This disconnect between the precipitation and lightning trends is attributed to lightning production being tied to development into the ice region [*Williams*, 1985]. Changes in precipitation, meanwhile, are dominated by warm rain processes closer to the surface [*Rosenfeld and Woodley*, 2003].

It is not immediately clear whether the TRMM-retrieved currents will favor El Niño or La Niña events. On the one hand, the passive microwave measurements that indicate convective vigor and cloud ice might favor El Niño conditions. On the other hand, smaller regions of near-surface rainfall during El Niño events might favor greater retrieved Wilson currents during La Niña conditions.

ENSO distributions of the TRMM-retrieved mean generator current are constructed using the Multivariate ENSO Index [MEI: *Wolter and Timlin*, 2011]. Negative MEI values correspond to La Niña events, while positive values correspond to El Niño events, and the amplitude of the index distinguishes their relative strengths. The

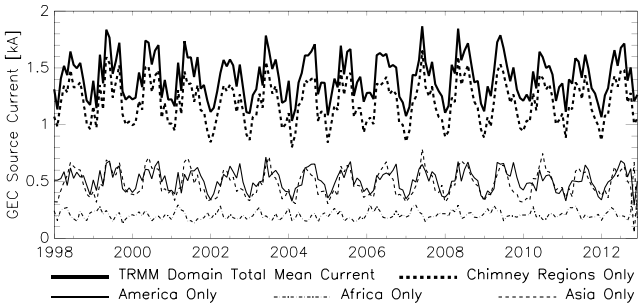

Figure 13. Fifteen year timeseries of the total TRMM-retrieved current. The greatest total current is produced during the summer months for the northern hemisphere, consistent with the GEC literature.

total mean TRMM-retrieved current as a function of MEI is shown in Figure 12. Aside from the strongest La Niña events that may not be representative, the strongest mean TRMM-retrieved currents are found when the MEI is close to zero. More pronounced El Niño or La Niña events lead to overall weaker currents. El Niño events may be associated with increased lightning, but the total TRMM-retrieved current is generally higher under La Niña conditions.

While the stronger thunderstorms over land during El Niño events may be more favorable for total lightning production, the TRMM-retrieved currents indicate that the size, intensity, location, and frequency of thunderstorms and ESCs all bear weight on the overall GEC response to ENSO. The neutral maximum suggests that the strongest generator currents can be achieved when tropical convection is not hindered by the limiting effects of either climate pattern. The La Niña preference in the total current, meanwhile, is likely tied to changes in shower cloud contributions that benefit from larger and more frequent - though weaker - storms. Finally, the ENSO response depends on the geographical region examined. The Americas and Asia chimneys show the largest change with MEI and reflect the global trend. African currents, on the other hand, increase slightly with the absolute value of MEI.

Though this ENSO response of the TRMM-retrieved generator current contrasts the El Niño preference for lightning from the literature, *Dowdy* [2016] points out that there are geographical and seasonal influences on the sign of the correlations between the ENSO indices and lightning flash densities. For example, positive NINO3.4 index anomalies (El Niño conditions) during the northern hemisphere Spring may lead to increases in lightning activity over China while positive values in the fall produce a decrease in lightning activity over Brazil. Moreover, correlation coefficients between NINO3.4 anomalies and flash densities over Indonesia are positive in the first half of the year and negative in the second half [*Dowdy*, 2016].

An in-depth analysis of the changes in the tropical chimneys with ENSO is beyond the scope of this study. Future work should also evaluate the joint response of the AC circuit (lightning) and DC circuit (Wilson currents) to ENSO events globally and in different regions of the world.

3.2.6. Decadal Variation of the TRMM-Retrieved Generator Current on a Decadal Time Scale

The final time scale that will be considered is the 15-year TRMM timeseries. Figure 13 shows how the total generator current fluctuated between 1998 and 2013. Despite fifteen years of annual cycles and ENSO events throughout this time period, the overall trend appears to be quite steady. The maximum variation of the annual total current is 7.5% in these 15 years. The annual cycle from Figure 11a can be noted for each year with a maximum total current in the northern hemisphere summer and minimum in the southern hemisphere summer, in agreement with the global temperature variation on annual time scales [*Williams*, 1994].

There is concern in the community that the GEC may be declining in time [summarized in *Williams*, 2009]. Our estimates of the total generator current that supplies the GEC do not appear to have changed since the launch of TRMM, even after the orbit boost in August of 2001 [*DeMoss and Bowman*, 2007]. It is important to note, however, that the TRMM record coincides with a time period of stable global mean surface temperatures and total lightning flash rates [*Williams et al.*, 2016]. For this reason, we reserve our judgment on the possibility of long-term change in the GEC generator current until the retrieval has been run on a record of sufficient length to capture such changes (~25 years).

3.2.7. Summary of the Variability of the Retrieved Generator Current

The variations in TRMM-retrieved generator current are summarized in Table 3 alongside similar measures for lightning adapted from the literature. Both the diurnal cycles and variations on decadal timescales agree with ranges provided for lightning. Diurnal variations in the TRMM-retrieved total current range from 34% for Universal Time to 58% for local time compared to 30-100% for lightning, while the decadal change is 7.5% compared to ~10% for lightning. The remaining time scales differ substantially, however. The variation of

Table 3. Variations in Lightning [Adapted From *Christian et al.*, 2003, *Bell et al.*, 2009, and *Williams*, 2005] and the Total TRMM-Derived Current on Discrete Time Scales

	Period [days]	Total Current Variation [%]	Lightning Variation [%]
Diurnal	1		~30-100
Universal Time		34	
Local Time		58	
Weekly	7	2	~15
MJO	30-60		~50
Amplitude		14	
Phase		13	
Semi-annual	182	110	~50
Annual	365	29	50-100
ENSO	1000-2000	25	10-100
Decadal	3000-5000	7.5	~10

the TRMM-retrieved generator current is greater than lightning on the semi-annual time scale (110% compared to ~50%) while it is smaller than lightning on the weekly (~2% compared to ~15%) and annual (29% compared to 50-100%) time scales. TRMM-retrieved currents are also less responsive to the MJO than lightning (~14% compared to ~50%). Though its variability with ENSO has a similar magnitude to lightning (25% compared to 10-100%), TRMM-retrieved currents are stronger in weak amplitude ENSO events. In more pronounced events, La Niña conditions generally produce stronger currents than El Niño conductions.

Contrasts between the variability of TRMM-retrieved total current and lightning activity suggest that thunderstorms and ESCs respond differently to these climate patterns. Electrified Shower cloud contributions have been shown to damp the diurnal cycle of lightning [*Mach et al.*, 2011] and thunderstorm rainfall [*Liu et al.*, 2010]. They similarly influence the variability of the total TRMM-retrieved current across all time scales considered. More work is needed to understand how the variation of the DC circuit (that includes these currents) connects with the variation of the AC circuit (that does not).

The issue at the center of this discussion is how electrified weather responds to the large-scale temperature perturbations [*Williams*, 2005, 1999] associated with these variations. This is also important in the context of climate looking ahead [*Williams and Mareev*, 2014]. The general variation of TRMM-retrieved current with the mean NCEP NCAR Reanalysis [*Kistler et al.*, 2001] surface temperature across the TRMM domain is shown in Figure 14. When the mean surface temperature of the tropics is between 18° C and 21° C, the total TRMM-retrieved current over the same region is around 1.4 kA. The total mean current increases with mean surface temperature between 21° C and 22.5° C, and then levels off at around 1.7 kA for temperatures up to 24° C. Lower currents can be noted for average temperatures below 18° C or above 24° C, but this is influenced by a limited sample size as indicated by increasing standard deviations.

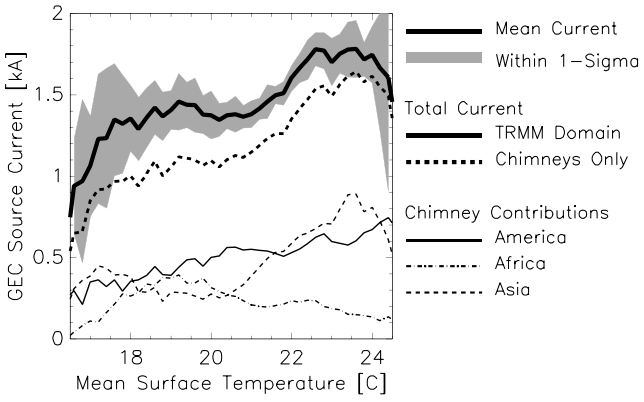

Figure 14. Variations in the total TRMM-retrieved current with the mean surface temperature across the TRMM domain.

To the extent that the data allow, the TRMM-retrieved generator current appears to increase or remain constant with increasing mean surface temperature in the tropics. In the absence of conductivity changes, we might expect no change or an increase in the total current produced by convective electrified weather with increasing temperatures rather than a decrease. Changes in current contributions vary by region. While the total current from the Americas and Asia chimneys increase with mean temperature, the total current from the African chimney decreases from ~350 A to ~100 A as

mean temperatures warm from 19° C. This behavior deviates from the diurnal and semi-annual cycles where the Africa contribution increased along with the Americas and Asia contributions in the warmer local afternoon (Figure 6a) and summer months (Figure 11b).

The decline of the African chimney is likely sparked by the local weather patterns that accompany these warmer temperatures rather than the temperature increase on its own. Higher mean temperatures across the tropics may not coincide with higher temperatures across the Africa chimney. An example of this is the annual cycle of the TRMM-retrieved current. Though current contributions from Africa increase with the length of time from the winter solstice (Figure 11b), maxima in the annual Africa curve (Figure 11a) occur in March and November rather than at a solstice. Further comparisons of the tropical chimneys and how their contributions vary with mean temperature warrant further investigation, but lie beyond the scope of this work.

3.3. Comment on the Role of Stratiform Clouds as Current Sources

The total current retrieved by the TRMM algorithm is most sensitive to the cloud types that are allowed to contribute current to the GEC. The most reasonable global mean retrieved currents and closest approximations to the Carnegie curve occur when electrified stratiform clouds are ignored even though ER-2 measurements show that electric fields and Wilson current contributions these clouds can be significant [*Deierling et al.*, 2014; *Peterson et al.*, 2015].

There are three possible factors that could explain why retrieved currents from electrified stratiform clouds are not well represented in the satellite retrieval. First, the retrieved electric fields (and, consequently, the current densities and total Wilson currents) may be overestimated in electrified stratiform regions. The oceanic stratiform example in *Peterson et al*. [2015] provides evidence for this argument. Second, the horizontal extent of the electrified stratiform cloud may be too large. Modest current densities integrated over a sizable area can lead to current contributions that overshadow the comparably small convective cores. Third, the algorithm has no mechanism to represent the polarity of the retrieved currents. Therefore, it cannot account for downward Wilson currents that would cancel out a fraction of the upward current. This issue affects the total current from convective clouds as well (see Table 2), but the prevalence of negative Wilson currents produced by inverted dipoles in stratiform clouds trailing squall lines [*Shepherd et al.*, 1996; *Williams*, 1998] and the EOSO that accompanies dissipating convection[*Marshall et al*., 2009] makes it primarily a stratiform issue.

Re-examinations of the convective and stratiform cases in the ER-2 data show good agreement with the measured electric field strengths over convective and stratiform clouds. Individual cases with large errors [i.e. the stratiform case in *Peterson et al.*, 2015] are usually oceanic and therefore subject to ocean artifacts that increase the electric fields across the overpass. The second issue of stratiform clouds being too large is also not likely to explain the stratiform bias. The algorithm only identifies the portion of the stratiform cloud with rainfall near the surface, thereby limiting this possible source of error.

The most likely candidate for the inconsistencies between the convective and stratiform total retrieved current with observations is the lack of polarity information provided by the algorithm. While *Mach et al*. [2010] indicates that 7% of the ER-2 overflights had observed negative (downward) Wilson currents, modeling results suggest that the majority of electrified stratiform clouds could produce negative currents [*Davydenko et al.*, 2011]. An alternate explanation for why the convective-only curves in Figure 2 produce the best agreements with the Carnegie curve is that ~50% of stratiform cloud current contributions are positive and ~50% are negative, and the total contribution is negligible compared to convection.

The role of stratiform cloud sources is tied to the larger issue of current contributions from Mesoscale Convective Systems (MCSs). MCSs are substantially larger and more organized than isolated convection. Model simulations indicate that they produce considerably stronger currents than typical storms [*Davydenko et al.*, 2004], though they are infrequent by comparison [*Nesbitt et al.*, 2000]. MCS's are also known to have a delayed diurnal cycle that peaks after midnight [*Laing*, 2003]. Since we do not distinguish between land and ocean sources in our local hour curves, MCS's also contribute to the morning peaks in Figure 6a. This delay has been proposed as evidence that isolated convection, rather than MCSs, is the primary driver of the GEC despite individually higher currents per storm from the latter. If MCSs played a larger role, then the Carnegie curve would also peak later than it does [*Williams and Mareev*, 2014].

The diurnal cycles of total convective and stratiform current in Figure 2 support this delayed response from MCSs. The diurnal cycle of current produced by convection peaks at 19:00 UTC compared to the 20:00 UTC

peak in the total current produced by all cloud types and the 21:00 UTC peak in the current produced by stratiform clouds. Though the retrieval is not well-suited for quantifying the stratiform contribution to the GEC, our Carnegie curve approximations provide evidence that the current contributions from ordinary and mesoscale convective features are reasonable.

4. Conclusion

The total generator current contributed to the GEC by electrified weather is estimated using a satellite version of the passive microwave electric field retrieval algorithm from *Peterson et al.* [2015] applied to TRMM and GPM observations. The total retrieved mean generator current is calculated to be 1.6 kA (1.4 kA if we assume that 7% of the total current is contributed by negative – downward – currents) and the diurnal cycle is found to be in excellent agreement with the Carnegie curve (1.7% RMS error using the optimal configuration of the algorithm). These retrieved currents include contributions from both thunderstorms and ESCs in land and ocean regions. Significant current contributions offshore signifies that oceanic convection and lightning-producing storms play an important role in the GEC.

The TRMM retrieval is used to examine variations in the total generator current on several time scales ranging from the diurnal cycle to a 15-year timeseries. The strongest variations in the retrieved current are on the semi-annual (110%), diurnal (local time: 58%), and annual (29%) time scales. Variations on ENSO timescales vary by as much as 25%, but our results indicate that - in contrast to lightning measurements - greater current is produced under neutral and La Niña conditions rather than during El Niño events. The MJO – both in terms of amplitude (14%) and phase (13%) – and decadal (7.5%), and weekly (2%) timescales show the least amount of variability. The global weekly cycle falls within the error bars of the estimated currents and does not appear to be robust.

This work highlights the need to clarify the role of stratiform cloud current sources for the GEC and to examine the AC and DC variations jointly. It also sets the stage for future work that will focus on examining Wilson current contributions from individual classes of storms – i.e. thunderstorms and shower clouds, isolated convection and MCS's – using Precipitation Features and assessing the responses of the individual chimney regions to weather and climate patterns.

Acknowledgments
This work was partly funded by the National Science Foundation Frontiers in Earth System Dynamics grant AGS-1135446 and NSF grant number 1519006. The National Center for Atmospheric Research is sponsored by the National Science Foundation. Data used in this study are hosted at Texas A&M University Corpus Christi and may be accessed at atmos.tamucc.edu/trmm/.

References

Adlerman, E. J., and E. R. Williams (1996), Seasonal variations of the global electrical circuit, *J. Geophys. Res.*, *101*, 29,679–29,688.
Albrecht, R. I., S. J. Goodman, D. E. Buechler, R. J. Blakeslee, and H. J. Christian (2016), Where are the lightning hotspots on Earth?, *Bull. Am. Meteorol. Soc.*, doi:10.1175/BAMS-D-14-00193.1.
Allen, R., J. Lindesay, and D. Parker (1996), *El Nino Southern Oscillation and Climate Variability*, CSIRO Publishing, Australia.
Altaratz, O., I. Koren, Y. Yair, and C. Price (2010), Lightning response to smoke from Amazonian fires, *Geophys. Res. Lett.*, *37*, L07801, doi:10.1029/2010GL042679.
Anyamba, E., E. R. Williams, J. Susskind, A. Fraser-Smith, and M. Fullekrug (2000), The manifestation of the Madden–Julian oscillation in global deep convection and in the Schumann resonance intensity, *J. Atmos. Sci.*, *57*, 1029–1044.
Awaka, J., T. Iguchi, and K. Okamoto (1998), Rain type classification algorithm, *Meas. Precipitation Space*, *3*, 213–224.
Bailey, J. C., R. J. Blakeslee, D. E. Buechler, and H. J. Christian (2007), Diurnal lightning distributions as observed by the Optical Transient Detector (OTD) and the Lightning Imaging Sensor (LIS), in *13th International Conference on Atmospheric Electricity*, Int. Comm. on Atmos. Electr., Beijing.
Baumgaertner, A. J., G. M. Lucas, J. P. Thayer, and S. A. Mallios (2014), On the role of non-electrified clouds in the Global Electric Circuit, *Atmos. Chem. Phys. Discuss.*, *14*, 9815–9847, doi:10.5194/acpd-14-9815-2014.
Bazilevskaya, G. A., et al. (2008), Cosmic ray-induced ion production in the atmosphere, *Space Sci. Rev.*, *137*(N1-4), doi:10.1007/s11214-008-9339-y.
Bell, T. L., D. Rosenfeld, and K.-M. Kim (2009), Weekly cycle of lightning: Evidence of storm invigoration by pollution, *Geophys. Res. Lett.*, *36*, L23805, doi:10.1029/2009GL040915.
Bell, T. L., D. Rosenfeld, K.-M. Kim, J.-M. Yoo, M.-I. Lee, and M. Hahnenberger (2008), Midweek increase in summer rain and storm heights suggests air pollution invigorates rainstorms, *J. Geophys. Res.*, *113*, D02209, doi:10.1029/2007JD008623.
Blakeslee, R. J., H. J. Christian, and B. Vonnegut (1989), Electrical measurements over thunderstorms, *J. Geophys. Res.*, *94*, 13,135–13,140.
Blakeslee, R. J., D. M. Mach, M. G. Bateman, and J. C. Bailey (2014), Seasonal variations in the lightning diurnal cycle and implications for the global electric circuit, *Atmos. Res.*, 135–136, doi:10.1016/j.atmosres.2012.09.023.
Blakeslee, R. J., et al. (1999), Diurnal lightning distribution as observed by the Optical Transient Detector (OTD), in *11th International Conference on Atmospheric Electricity*, NASA Conf. Publ., NASA/CP-1999-209261, pp. 742–745.
Burns, G. B., A. V. Frank-Kamenetsky, O. A. Troschichev, E. A. Bering, and B. D. Reddell (2005), Interannual consistency of bi-monthly differences in annual variations of the ground-level, vertical electric field, *J. Geophys. Res.*, *110*, D10106, doi:10.1029/2004JD005469.
Burns, G. B., B. A. Tinsley, A. V. Frank-Kamenetsky, O. A. Troshichev, W. J. R. French, and A. R. Klekociuk (2012), Monthly diurnal global atmospheric circuit estimates derived from Vostok electric field measurements adjusted for local meteorological and solar wind influences, *J. Atmos. Sci.*, *69*, 2061–2082, doi:10.1175/JAS-D-11-0212.1.

Burns, G. B., A. V. Frank-Kamenetsky, B. A. Tinsley, W. J. R. French, P. Grigioni, D. Camporeale, and E. A. Bering (2017), Atmospheric global circuit variations from Vostok and Concordia electric field measurements, *J. Atmos. Sci.*, *74*, 783–800, doi:10.1175/JAS-D-16-0159.1.

Cecil, D. J., D. E. Buechler, and R. J. Blakeslee (2014), Gridded lightning climatology from TRMM-LIS and OTD: Dataset description, *Atmos. Res.*, *135–136*, 404–414.

Christian, H. J., et al. (2003), Global frequency and distribution of lightning as observed from space by the Optical Transient Detector, *J. Geophys. Res.*, *108*(D1), 4005, doi:10.1029/2002JD002347.

Cordisco, E., C. Prigent, and F. Aires (2006), Snow characterization at a global scale with passive microwave satellite observations, *J. Geophys. Res.*, *111*, D19102, doi:10.1029/2005JD006773.

Davydenko, S. S., E. A. Mareev, T. C. Marshall, and M. Stolzenburg (2004), On the calculation of electric fields and currents ofmesoscale convective systems, *J. Geophys. Res.*, *109*, D11103, doi:10.1029/2003JD003832.

Davydenko, S. S., T. C. Marshall, and M. Stolzenburg (2011), Modeling the electric properties of MCS stratiform regions and their contribution to the global circuit, Rio de Janeiro, Brazil, 07–12 Aug.

Deierling, W., C. Kalb, D. Mach, C. Liu, M. Peterson, and R. Blakeslee (2014), On the Variability of Wilson Currents by Storm Type and Phase, 15th International Conference on Atmospheric Electricit, Normal, OK. [Available online at http://www.nssl.noaa.gov/users/mansell/icae2014/preprints/Deierling_77.pdf.]

DeMoss, J., and K. Bowman (2007), Changes in TRMM Rainfall due to the Orbit Boost Estimated from Buoy Rain Gauge Data, *J. Atmos. Oceanic Technol.*, *24*, 1598–1607, doi:10.1175/JTECH2082.1.

Dobson, J. E., E. A. Bright, P. R. Coleman, R. C. Durfee, and B. A. Worley (2000), LandScan: A global population database for estimating populations at risk, *Photogramm. Eng. Remote. Sens.*, *2000*, 849–857.

Dowdy, A. J. (2016), Seasonal forecasting of lightning and thunderstorm activity in tropical and temperate regions of the world, *Sci. Rep.*, *6*, 20,874, doi:10.1038/srep20874.

Dye, J. E., et al. (2007), Electric fields, cloud microphysics, and reflectivity in anvils of Florida thunderstorms, *J. Geophys. Res.*, *112*, D11215, doi:10.1029/2006JD007550.

Füllekrug, M., and S. Constable (2000), Global triangulation of intense lightning discharges, *Geophys. Res. Lett.*, *27*, 333.

Hamid, E. Y., Z.-I. Kawasaki, and R. Mardiana (2001), Impact of the 1997–98 El Nino events on lightning activity over Indonesia, *Geophys. Res. Lett.*, *28*, 147–150.

Harrison, R. G. (2002), Twentieth century secular decrease in the atmospheric potential gradient, *Geophys. Res. Lett.*, *29*(14), 1660, doi:10.1029/2002GL014878.

Harrison, R. G. (2013), The Carnegie curve, *Surv. Geophys.*, *34*, 209–232, doi:10.1007/s10712-012-9210-2.

Hendon, H., and K. Woodberry (1993), The diurnal cycle of tropical convection, *J. Geophys. Res.*, *58*, 16 623–16 637.

Hou, A., R. Kakar, S. Neeck, A. Azarbarzin, C. Kummerow, M. Kojima, R. Oki, K. Nakamura, and T. Iguchi (2014), The Global Precipitation Measurement Mission, *Bull. Am. Meteorol. Soc.*, *95*, 701–722, doi:10.1175/BAMS-D-13-00164.1.

Hutchins, M. L., R. H. Holzworth, and J. B. Brundell (2014), Diurnal variation of the global electric circuit from clustered thunderstorms, *J. Geophys. Res. Space Physics*, *119*, 620–629, doi:10.1002/2013JA019593.

Iguchi, T., T. Kozu, R. Meneghini, J. Awaka, and K. Okamoto (2000), Rain-profiling algorithm for the TRMM precipitation radar, *J. Appl. Meteorol.*, *39*, 2038–2052.

Israel, H. (1973), Atmospheric Electricity, Vol. II. Israel Program for Scientific Translations, Ltd., 0 7065 1129 8.

Jayaratne, E. R., C. P. R. Saunders, and J. Hallet (1983), Laboratory studies of the charging of soft hail during ice crystal interactions, *Q. J. R. Meteorol. Soc.*, *109*, 609–630.

Kalb, C. P., W. D. Deierling, A. Baumgaertner, M. J. Peterson, C. Liu, and D. Mach (2016), Parameterizing total storm conduction currents in the Community Earth System Model, *J. Geophys. Res. Atmos.*, *121*, 13,715–13,734, doi:10.1002/2016JD025376.

Kistler, R., et al. (2001), The NCEP–NCAR 50-Year Reanalysis: Monthly means CD-ROM and documentation, *Bull. Am. Meteorol. Soc.*, *82*, 247–267.

Kummerow, C., W. Barnes, T. Kozu, J. Shiue, and J. Simpson (1998), The Tropical Rainfall Measuring Mission (TRMM) sensor package, *J. Atmos. Oceanic Technol.*, *15*, 809–817.

Laing, A. G. (2003), Mesoscale meteorology/mesoscale convective systems, in *Encyclopedia of Atmospheric Sciences*, edited by J. R. Holton, pp. 1251–1261, Academic Press, London.

Lang, T. J., S. A. Rutledge, and K. C. Wiens (2004), Origins of positive cloud-to-ground lightning flashes in the stratiform region of a mesoscale convective system, *Geophys. Res. Lett.*, *31*, L10105, doi:10.1029/2004GL019823.

Liu, C., and E. J. Zipser (2008), Diurnal cycles of precipitation, clouds, and lightning in the tropics from 9 years of TRMM observations, *Geophys. Res. Lett.*, *35*, L04819, doi:10.1029/2007GL032437.

Liu, C., E. J. Zipser, D. J. Cecil, S. W. Nesbitt, and S. Sherwood (2008), A cloud and precipitation feature database from 9 years of TRMM observations, *J. Appl. Meteorol. Climate*, *47*, 2712–2728, doi:10.1175/2008JAMC1890.

Liu, C., E. R. Williams, E. J. Zipser, and G. Burns (2010), Diurnal variations of global thunderstorms and electrified shower clouds and their contribution to the global electric circuit, *J. Atmos. Sci.*, *67*, 309–323, doi:10.1175/2009JAS3248.1.

Lucas, G. M., A. J. G. Baumgaertner, and J. P. Thayer (2015), A Global Electric Circuit Model within a Community Climate Model, *J. Geophys. Res. Atmos.*, *120*, 12,054–12,066, doi:10.1002/2015JD023562.

Lyons, W. A., T. E. Nelson, E. R. Williams, J. Cramer, and T. Turner (1998), Enhanced positive cloud-to-ground lightning in thunderstorms ingesting smoke, *Science*, *282*, 77–81.

Mach, D. M., R. J. Blakeslee, M. G. Bateman, and J. C. Bailey (2009), Electric fields, conductivity, and estimated currents from aircraft overflights of electrified clouds, *J. Geophys. Res.*, *114*, D10204, doi:10.1029/2008JD011495.

Mach, D. M., R. J. Blakeslee, M. G. Bateman, and J. C. Bailey (2010), Comparisons of total currents based on storm location, polarity, and flash rates derived from high-altitude aircraft overflights, *J. Geophys. Res.*, *115*, D03201, doi:10.1029/2009JD012240.

Mach, D. M., R. J. Blakeslee, and M. G. Bateman (2011), Global electric circuit implications of combined aircraft storm electric current measurements and satellite-based diurnal lightning statistics, *J. Geophys. Res.*, *116*, D05201, doi:10.1029/2010JD014462.

Madden, R. A., and P. R. Julian (1972), Description of global-scale circulation cells in the Tropics with a 40–50 day period, *J. Atmos. Sci.*, *29*, 1109–1123.

Mansell, E. R., D. R. MacGorman, C. L. Ziegler, and J. M. Straka (2005), Charge structure and lightning sensitivity in a simulated multicell thunderstorm, *J. Geophys. Res.*, *110*, D12101, doi:10.1029/2004JD005287.

Märcz, F., and R. G. Harrison (2003), Long-term changes in atmospheric electrical parameters observed at Nagycenk (Hungary) and the UK observatories at Eskdalemuir and Kew, *Ann. Geophys.*, *21*, 2193–2200.

Mareev, E. A., and E. M. Volodin (2014), Variation of the global electric circuit and Ionospheric potential in a general circulation model, *Geophys. Res. Lett.*, *41*, 9009–9016, doi:10.1002/2014GL062352.

Mareev, E. A., S. A. Yashunin, S. S. Davydenko, T. C. Marshall, M. Stolzenburg, and C. R. Maggio (2008), On the role of transient currents in the global electric circuit, *Geophys. Res. Lett.*, *35*, L15810, doi:10.1029/2008GL034554.
Markson, R. (2007), The global circuit intensity: Its measurement and variation over the last 50 years, *Bull. Am. Meteorol. Soc.*, doi:10.1175/BAMS-88-2-223,223-241.
Marshall, T. C., and W. C. Rust (1993), Two types of vertical electrical structures in stratiform precipitation regions of mesoscale convective systems, *Bull. Am. Meteorol. Soc.*, *74*, 2159–2170.
Marshall, T. C., M. Stolzenburg, P. R. Krehbiel, N. R. Lund, and C. R. Maggio (2009), Electrical evolution during the decay stage of New Mexico thunderstorms, *J. Geophys. Res.*, *114*, D02209, doi:10.1029/2008JD010637.
Mezuman, K., C. Price, and E. Galanti (2014), On the spatial and temporal distribution of global thunderstorm cells, *Environ. Res. Lett.*, *9*, 124023, 9, doi:10.1088/1748-9326/9/12/124023.
Nesbitt, S. W., and E. J. Zipser (2003), The diurnal cycle of rainfall and convective intensity according to three years of TRMM measurements, *J. Clim.*, *16*, 14561475.
Nesbitt, S. W., E. J. Zipser, and D. J. Cecil (2000), A census of precipitation features in the tropics using TRMM: Radar, ice scattering, and lightning observations, *J. Clim.*, *13*, 4087–4106.
Nicoll, K. A., and R. G. Harrison (2016), Stratiform cloud electrification: comparison of theory with multiple in-cloud measurements, *Q. J. R. Meteorol. Soc.*, *142*, 2679–2691, doi:10.1002/qj.2858.
Peterson, M., C. Liu, D. Mach, W. Deierling, and C. Kalb (2015), A Method of Estimating Electric Fields above Electrified Clouds from Passive Microwave Observations, *J. Atmos. Oceanic Technol.*, *32*, 1429–1446, doi:10.1175/JTECH-D-14-00119.1.
Philander, S. G. (1990), *El Nino, La Nina and the Southern Oscillation*, *International Geophysical Series*, vol. 46, 293 pp., Academic Press, San Diego, London.
Price, C. (2009), Will a drier climate result in a more lightning?, *Atmos. Res.*, *91*, 479–484.
Reeve, N., and R. Toumi (1999), Lightning activity as an indicator of climate change, *J. R. Meteorol. Soc.*, *125*, 893–903.
Reynolds, S. E., M. Brook, and M. F. Gourley (1957), Thunderstorm charge separation, *J. Meteorol.*, *14*(5), 163–178.
Roble, R. G., and I. Tzur (1986), The global atmospheric–electrical circuit, in *The Earth's Electrical Environment*, edited by E. P. Krider and R. G. Roble, pp. 206–231, Nat. Acad. Press, Washington.
Romatschke, U., and R. A. Houze (2011), Characteristics of Precipitating Convective Systems in the South Asian Monsoon, *J. Hydrometeorol.*, *12*, 3–26, doi:10.1175/2010JHM1289.1.
Rosenfeld, D., and W. L. Woodley (2003), Closing the 5-year circle: From cloud seeding to space and back to climate change through precipitation physics, in *Cloud Systems, Hurricanes, and the Tropical Rainfall Measuring Mission (TRMM), Meteorol. Monogr.*, chap. 6, pp. 59–80, *Am. Meteorol. Soc.*
Rosenfeld, D., and T. L. Bell (2011), Why do tornados and hailstorms rest on weekends?, *J. Geophys. Res.*, *116*, D20211, doi:10.1029/2011JD016214.
Rosenfeld, D., E. Williams, M. O. Andreae, E. Freud, U. Pöschl, and N. O. Rennó (2012), The scientific basis for a satellite mission to retrieve CCN and its impacts on convective clouds, *Atmos. Meas. Tech.*, *5*, 2039–2055. [Available at www.atmos-meas-tech.net/5/2039/2012/doi:10.5194/amt-5-2039-2012.]
Rycroft, M. J., and R. G. Harrison (2012), Electromagnetic atmospheric-plasma coupling: the global atmospheric electric circuit, *Space Sci. Rev.*, *137*(N1-4), 363–384, doi:10.1007/s11214-011-9830-8.
Rycroft, M. J., S. Israelsson, and C. Price (2000), The global atmospheric electric circuit, solar activity and climate change, *J. Atmos. Sol. Terr. Phys.*, *62*, 1563–1576.
Rycroft, M. J., A. Odzimek, N. F. Arnold, M. Fullekrug, A. Kulak, and T. Neubert (2007), New model simulations of the global atmospheric electric circuit driven by thunderstorms and electrified shower clouds: The roles of lightning and sprites, *J. Atmos. Sol. Terr. Phys.*, *69*(17-18), 2,485–2,509.
Sátori, G., E. Williams, and I. Lemperger (2009), Variability of global lightning activity on the ENSO time scale, *Atmos. Res.*, *91*, 500–507.
Saunders, C. P. R., and S. L. Peck (1998), Laboratory studies of the influence of the rime accretion rate on charge transfer during crystal/graupel collisions, *J. Geophys. Res.*, *103*, 13,949–13,956.
Saunders, C. P. R., W. D. Keith, and R. P. Mitzeva (1991), The effect of liquid water content on thunderstorm charging, *J. Geophys. Res.*, *96*, 11,007–11,017.
Shepherd, T. R., W. D. Rust, and T. C. Marshall (1996), Electric Fields and Charges near 0°C in Stratiform Clouds, *Mon. Weather Rev.*, *124*, 919–938, doi:10.1175/1520-0493(1996)124<0919:EFACNI>2.0.CO;2.
Shimizu, S., R. Oki, T. Tagawa, T. Iguchi, and M. Hirose (2009), Evaluation of the effects of the orbit boost of the TRMM satellite on PR rain estimates, *J. Meteorol. Soc. Jpn.*, *87A*, 83–92.
Shin, D.-B., and L. S. Chiu (2008), Effects of TRMM boost on oceanic rainfall estimates based on microwave emission brightness temperature histograms (METH), *J. Atmos. Oceanic Technol.*, *25*, 1888–1893.
Smith, E. A., et al. (2007), International global precipitation measurement (GPM) program and mission: An overview, in *Measuring Precipitation From Space*, pp. 611–653, Springer, Netherlands.
Spencer, R. W., H. G. Goodman, and R. E. Hood (1989), Precipitation retrieval over land and ocean with the SSM/I: Identification and characteristics of the scattering signal, *J. Atmos. Oceanic Technol.*, *6*, 254–273.
Spencer, R. W., R. E. Hood, F. J. LaFontaine, E. A. Smith, R. Platt, R. J. Galliano, V. L. Griffin, and E. Lobl (1994), High Resolution Imaging of Rain Systems with the Advanced Microwave Precipitation Radiometer, *J. Atmos. Oceanic Technol.*, *11*(4), 849–857.
Stolzenburg, M., T. C. Marshall, W. D. Rust, and B. F. Smull (1994), Horizontal distribution of electrical and meteorological conditions across the stratiform region of a mesoscale convective system, *Mon. Weather Rev.*, *122*, 1777–1797.
Takahashi, T. (1978), Riming electrification as a charge generation mechanism in thunderstorms, *J. Atmos. Sci.*, *35*, 1536–1548.
Takahashi, T., and K. Miyawaki (2002), Reexamination of riming electrification in a wind tunnel, *J. Atmos. Sci.*, *59*(5), 1018–1025.
Tinsley, B. A., and L. Zhou (2006), Initial results of a global circuit model with variable stratospheric and tropospheric aerosols, *J. Geophys. Res.*, *111*, D16205, doi:10.1029/2005JD006988.
Vonnegut, B., D. J. Latham, C. B. Moore, and S. J. Hunyady (1995), An explanation for anomalous lightning from forest fire clouds, *J. Geophys. Res.*, *100*, 5037–5050.
Wheeler, M. C., and H. Hendon (2004), An all-season real-time multivariate MJO index: Development of an index for monitoring and prediction, *Mon. Weather Rev.*, *122*, 1917–1931.
Whipple, F. J. W. (1929), On the association of the diurnal variation of electric potential gradient in fine weather with the distribution of thunderstorms over the globe, *Q. J. R. Meteorol. Soc.*, *55*, 1–17.
Whipple, F. J. W., and F. J. Scrase (1936), Point discharge in the electric field of the earth, *Geophys. Mem*, *68*(7), 1–20.

Williams, E., D. Rosenfeld, N. Madden, C. Labrada, J. Gerlach, and L. Atkinson (1999), The role of boundary layer aerosol in the vertical development of precipitation and electrification: Another look at the contrast in lightning over land and over ocean, 11th International Conference on Atmospheric Electricity, Guntersville, Alabama, 7-11 June.

Williams, E. R. (1985), Large-scale charge separation in thunderclouds, *J. Geophys. Res.*, *90*, 6013–6025.

Williams, E. R. (1992), The Schumann resonance: A global tropical thermometer, *Science*, *256*, 1184–1187.

Williams, E. R. (1994), Global circuit response to seasonal variations in global surface air temperature, *Mon. Weather Rev.*, *122*, 1917–1929.

Williams, E. R. (1998), The positive charge reservoir for sprite-producing lightning, *J. Atmos. Sol. Terr. Phys.*, *60*(7), 689–692, doi:10.1016/S1364-6826(98)00030-3.

Williams, E. R. (1999), Global circuit response to temperature on distinct time scales: A status report, in *Atmospheric and Ionospheric Phenomena Associated with Earthquakes*, edited by M. Hayakawa, Terra Scientific Publishing, Tokyo.

Williams, E. R. (2003), Comment to "Twentieth century secular decrease in the atmospheric potential gradient" by Giles Harrison, *Geophys. Res. Lett. 30*(15), 1803, doi:10.1029/2003GL017094.

Williams, E. R. (2005), Lightning and climate: A review, *Atmos. Res.*, *76*, 272–287.

Williams, E. R. (2009), The global electrical circuit: A review, *Atmos. Res.*, *91*(2–4), 140–152, doi:10.1016/j.atmosres.2008.05.018.

Williams, E. R., and S. J. Heckman (1993), The local diurnal variation of cloud electrification and the global diurnal variation of negative charge on the Earth, *J. Geophys. Res.*, *98*, 5221–5234.

Williams, E. R., and G. Satori (2004), Lightning, thermodynamic and hydrological comparison of the two tropical continental chimneys, *J. Atmos. Sol. Terr. Phys.*, *66*, 1213–1231.

Williams, E. R., and E. Mareev (2014), Recent progress on the global electric circuit, *J. Atmos. Res.*, *135–136*, 208–227.

Williams, E. R., M. E. Weber, and R. E. Orville (1989), The relationship between lightning type and convective state of thunderclouds, *J. Geophys. Res.*, *94*, 13,213–13,220.

Williams, E. R., et al. (2010), Ground-based detection of sprites and their parent lightning flashes over Africa during the 2006 AMMA campaign, *Q. J. R. Meteorol. Soc.*, *136*, 257–271, doi:10.1002/qj.489.

Williams, E. R., A. Guha, R. Boldi, H. Christian, and D. Buechler (2016), Global lightning activity and the hiatus in global warming. *World Meeting on Lightning*, Cartagena de Indias, Colombia. [Available at http://www.acofi.edu.co/womel/wp-content/uploads/2016/04/Earle-R.-Williams.pdf.]

Wilson, C. T. R. (1920), Investigation on lightning discharges and on the electric field of thunderstorms, *Phil. Trans. R. Soc. Ser. A.*, *221*, 73–115.

Wolter, K., and M. S. Timlin (2011), El Niño/Southern Oscillation behaviour since 1871 as diagnosed in an extended multivariate ENSO index (MEI.ext), *Int. J. Climatol.*, *31*, 1074–1087.

Yoshida, S., T. Morimoto, T. Ushio, and Z. Kawasaki (2007), ENSO and convective activities in South-East Asia and Western Pacific, *Geophys. Res. Lett.*, *34*, L21806, doi:10.1029/2007GL030758.

Yoshida, S., T. Morimoto, T. Ushio, and Z. Kawasaki (2009), A fifth-power relationship for lightning activity from Tropical Rainfall Measuring Mission satellite observations, *J. Geophys. Res.*, *114*, D09104, doi:10.1029/2008JD010370.